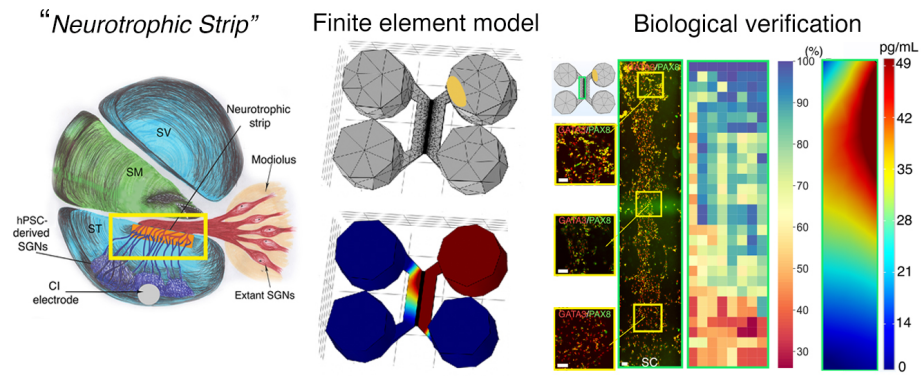


# Graphical Abstract

## Developing the Bioactive Cochlear Implant: Bridging the electrode–neuron gap through neurite guidance

Kevin T. Nella, Benjamin M. Norton, Hsiang-Tsun Chang, Rachel A. Heuer,  
Christian B. Roque, Akihiro J. Matsuoka



# Developing the Bioactive Cochlear Implant: Bridging the electrode–neuron gap through neurite guidance

Kevin T. Nella<sup>a,b</sup>, Benjamin M. Norton<sup>a</sup>, Hsiang-Tsun Chang<sup>a</sup>, Rachel A. Heuer<sup>a</sup>, Christian B. Roque<sup>a</sup>, Akihiro J. Matsuoka<sup>a,c,d,e,\*</sup>

<sup>a</sup>*Department of Otolaryngology–Head and Neck Surgery, Feinberg School of Medicine, Northwestern University, Chicago IL, 60611, USA*

<sup>b</sup>*Department of Mechanical Engineering, Robert R. McCormick School of Engineering and Applied Science, Northwestern University, Evanston, IL., USA*

<sup>c</sup>*Simpson Querrey Institute, Chicago IL, 60611, USA*

<sup>d</sup>*Roxelyn and Richard Pepper Department of Communication Sciences and Disorders, School of Communication, Northwestern University, Evanston, IL., 60210, USA*

<sup>e</sup>*The Hugh Knowles Center for Clinical and Basic Science in Hearing and its Disorders, Evanston, IL. 60210, USA*

---

## Abstract

Although cochlear implant (CI) technology has allowed partial restoration of hearing over the last few decades, persistent challenges remain - including the deciphering of rich acoustic signals into a digital pulse-train signal. Among these challenges, the “electrode–neuron gap” poses the most significant obstacle to advancing past the current plateau in CI performance. Resulting issues include limited performance in noisy environments and a poor ability to decode intonation and music. We propose the development of a “neurotrophic strip”—a biological interface that doubly preserves endogenous spiral ganglion neurons (SGNs) while precisely directing the growth of neurites arising from transplanted human pluripotent stem cell (hPSC)-derived otic neuronal progenitors (ONPS), toward endogenous SGNs. We hypothesized that the Polyhedrin Delivery System (PODS®-human brain-derived neurotrophic factor [BDNF]) could stably

---

\*Corresponding author: Akihiro J. Matsuoka, Department of Otolaryngology–Head and Neck Surgery, Feinberg School of Medicine, Northwestern University, 676 North St. Clair Street Suite 1325, Chicago, IL 60611, USA. E-mail addresses: amatsuok@nm.org, akihiro.matsuoka@northwestern.edu.

Email addresses: kevin.nella@northwestern.edu (Kevin T. Nella), benjamin.norton@northwestern.edu (Benjamin M. Norton), hsiangtsun.chang@gmail.com (Hsiang-Tsun Chang), racheuer@gmail.com (Rachel A. Heuer), christian.b.roq@gmail.com (Christian B. Roque), amatsuok@nm.org (Akihiro J. Matsuoka)

provide an adequate BDNF gradient to hPSC-derived ONPs, thereby simultaneously facilitating otic neuronal differentiation and directional neurite outgrowth. To test this hypothesis, we first devised a finite element model to simulate the *in vitro* BDNF gradient generated by PODS®. For biological verification, we validated the concept of the neurotrophic strip by using a multi-chamber microfluidic device, which mimics the *in vivo* micro-environment more accurately than conventional laboratory plates in terms of volume and concentrations of endogenous/exogenous factors. We were able to generate the optimal BDNF concentration gradient to enable survival, neuronal differentiation toward hPSC-derived SGNs, and directed neurite extension of hPSC-derived SGNs. The technique will allow us to further advance our concept of the “neurotrophic strip” by controlling neurite direction of transplanted hPSC-derived ONPs. This proof-of-concept study provides a step toward the next generation of CI technology.

*Keywords:* human pluripotent stem cells, finite element model, microfluidic device, neurotrophic factor, cochlear implant, neuroelectric interface, stem cell niche, spiral ganglion neurons

*2010 MSC:* 74S05, 62P10, 92C20

---

<sup>1</sup> **1. Introduction**

<sup>2</sup> The cochlear implant (CI), which provides functional restoration in patients  
<sup>3</sup> with sensorineural hearing loss, forms a neuro-electronic interface with the pe-  
<sup>4</sup> ripheral auditory nervous system [1]. CI technology functions by electrically  
<sup>5</sup> stimulating the extant population of auditory neurons (i.e., spiral ganglion neu-  
<sup>6</sup> rons [SGNs]). Although CI technology has allowed partial restoration of hearing  
<sup>7</sup> for this patient population over the last few decades, persistent challenges, in-  
<sup>8</sup> cluding the deciphering of rich acoustic signals into digital pulse-train signals,  
<sup>9</sup> remain. Among these challenges, the “electrode-neuron gap” poses the most  
<sup>10</sup> significant obstacle to advancing past the current plateau in CI performance.  
<sup>11</sup> This phenomenon symptomatically manifests as limited performance in noisy  
<sup>12</sup> environments and poor ability to decode intonation and music [2], arguably de-  
<sup>13</sup> creasing quality of life. The gap exists between the CI electrode and the target  
<sup>14</sup> membranes of dendrites in surviving endogenous SGNs [3]. It results in the  
<sup>15</sup> requirement of larger CI excitation fields, leading to current spread that excites  
<sup>16</sup> and therefore disables the neighboring electrodes, resulting in fewer information  
<sup>17</sup> channels to the brain, all within discrete time steps [2, 4]. This can develop into  
<sup>18</sup> a vicious cycle as fewer information channels to the brain also prompt the need  
<sup>19</sup> for larger CI excitation fields. The length of the gap generally spans hundreds of  
<sup>20</sup>  $\mu\text{m}$  [5, 6]. Hahnewald et al. demonstrated *in vitro* that energy needed to elicit  
<sup>21</sup> a response can be reduced by up to 20% by reducing the distance from 40 to  
<sup>22</sup> zero  $\mu\text{m}$  (by growing early postnatal mouse SGN explants on a microelectrode  
<sup>23</sup> array) [4].

<sup>24</sup> Previous work has introduced the concept of a “bioactive” CI to resolve the  
<sup>25</sup> electrode-neuron gap *in vivo*[7, 8, 9]. The bioactive CI combines the current  
<sup>26</sup> state-of-the-art CI technology with emerging stem cell-replacement therapy in  
<sup>27</sup> the inner ear. In this scheme, transplanted human pluripotent stem cell (hPSC)-  
<sup>28</sup> derived SGNs bridge the gap between the CI electrode and surviving endogenous  
<sup>29</sup> SGNs. Furthermore, introducing neurotrophin gradients has been shown to  
<sup>30</sup> guide hPSC grafts in spinal cord injury [10], direct growth of endogenous SGNs

31 toward CI electrodes in the scala tympani [11], and enable transplanted hPSC  
32 derived otic neuronal progenitors (ONPs) to grow neurites toward the modio-  
33 lus [9]. Although promising, these studies failed to observe adequate directed  
34 neurite outgrowth toward endogenous SGNs (i.e., lack of synaptic connections  
35 between hPSC grafts and endogenous SGNs), presumably preventing significant  
36 improvements in functional recovery of hearing.

37 To confront this issue, we propose the development of a “neurotrophic strip”—a  
38 biological interface that doubly preserves endogenous SGNs and precisely directs  
39 the growth of neurites arising from transplanted hPSC-derived ONPs toward  
40 the endogenous SGNs. The highlighted yellow-square area in Figure 1A shows  
41 a schematic diagram of this concept. Here, the neurotrophic strip (shown as  
42 an orange rectangle in Figure 1A) stimulates neurite outgrowth from both the  
43 hPSC-derived ONPs and the endogenous SGNs via a neurotrophic factor gra-  
44 dient [12]. While the concept of using a neurotrophin gradient for directional  
45 axonal growth has existed for a few decades, incorporation of neurotrophin gra-  
46 dients with any tissue- or bio-engineered scaffold has been extremely challenging  
47 due to the lack of self-sustaining neurotrophin delivery methods—their eventual  
48 depletion triggers an accelerated decline in neurite growth and survival of extant  
49 SGNs [13, 14, 15]. One major contributor is the structurally unstable nature of  
50 neurotrophins, which suffer from fragility and thermo-instability under normal  
51 physiological conditions both *in vitro* and *in vivo*, leading to short half-lives  
52 typically ranging from minutes to hours [16]. We set out to mitigate this phe-  
53 nomenon by utilizing the polyhedrin delivery system (PODS®)—a crystalline  
54 growth factor formulation developed to enable long-term release of growth fac-  
55 tors (e.g., neurotrophins) [17, 18, 19] (Figure 1B). The PODS® technology has  
56 adapted viral machinery to encase a chosen growth factor into polyhedrin pro-  
57 tein cases. The resultant growth factor co-crystals have slow degradation profiles  
58 under physiological conditions and, therefore, allow the sustained release of em-  
59 bedded bioactive growth factors.

60 We reasoned that a bio-engineered scaffolding incorporated with PODS®  
61 technology can establish a neuronal network between transplanted hPSC-derived

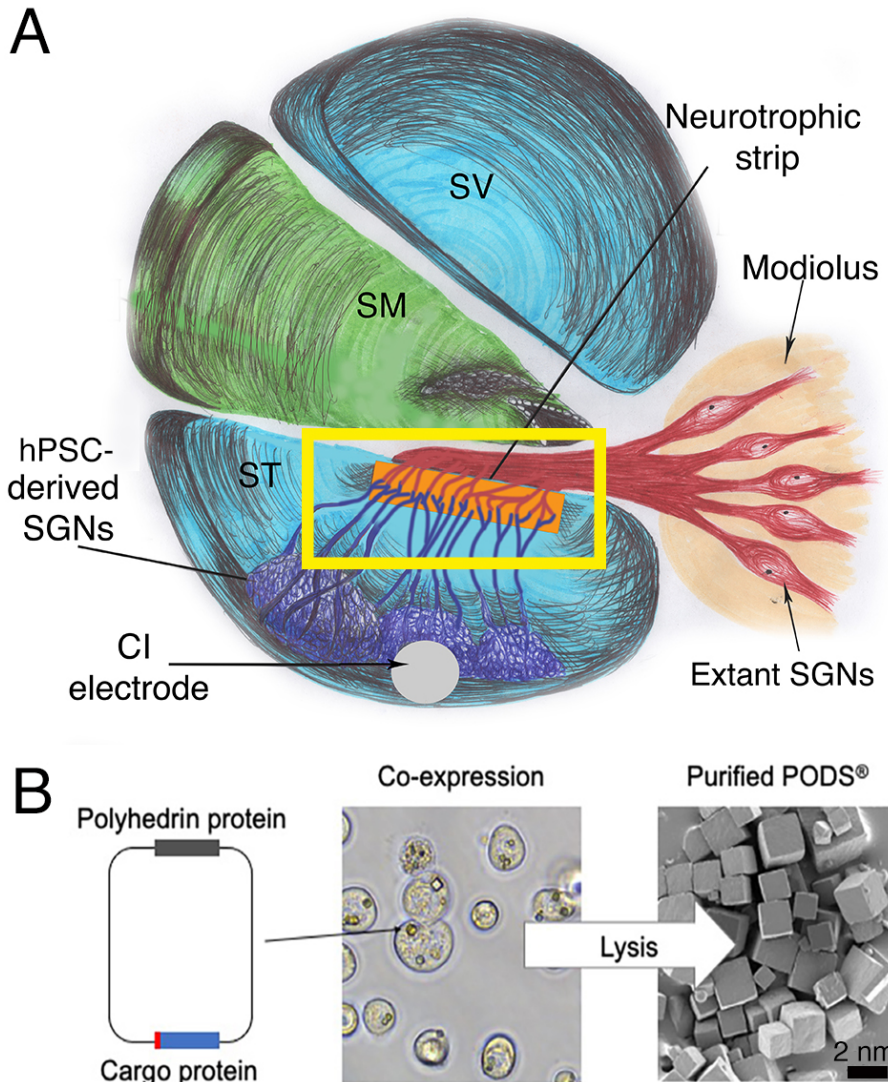


Figure 1: (A): A next-generation bioactive CI and a neurotrophic strip. The neural network in this scheme consists of a CI electrode, transplanted stem cell-derived SGNs, the neurotrophic strip, and extant/endogenous SGNs (red). Note that neuronal connection is largely absent with hair cells (not shown). (B): Polyhedrin Delivery System (PODS)<sup>®</sup>. PODS<sup>®</sup> crystals are cubic protein co-crystals produced by Sf9 cells (a clonal isolate of *Spodoptera frugiperda* Sf21 cells [IPLB-Sf21-AE], in which the polyhedrin protein and a second protein are co-expressed). This second protein is termed as the active, or cargo protein (Figure 1B, left). Inside the Sf9 cells, polyhedrin proteins self-assemble into cubic crystals (Figure 1B, center) while the active protein, tagged with a short peptide sequence, binds to the growing polyhedrin crystal. The crystals are extracted and purified by simple cell lysis and washes to remove cell debris (Scanning electron micrograph, Figure 1B, right).

62 ONP grafts and extant SGNs in the inner ear. More specifically, we hypothe-  
63 sized that PODS®-recombinant human neurotrophin system could stably pro-  
64 vide and maintain an adequate neurotrophin gradient to facilitate otic neuronal  
65 differentiation of and directional neurite outgrowth from hPSC-derived ONPs, .  
66 To test this hypothesis, we first devised a finite element model (FEM) to simu-  
67 late the *in vitro* neurotrophin gradient generated by PODS®. In this study, we  
68 focus on the role of BDNF—the most studied of the neurotrophins in the inner  
69 ear, and the most vital for the functional recovery of damaged SGNs [20]. For  
70 biological validation and demonstration we used a multi-chamber microfluidic  
71 device, that which mimics the *in vivo* micro-environment of the inner ear more  
72 so than conventional laboratory plates in terms of volume and concentrations  
73 of endogenous/exogenous factors [21].

74 **2. Materials and Methods**

75 *2.1. Polyhedrin delivery system*

76 The Polyhedrin Delivery System (PODS®-human BDNF [rhBDNF]) (Cell  
77 Guidance Systems, Cambridge, United Kingdom) was used as a self sustain-  
78 ing source of rhBDNF. PODS®-rhBDNF is composed of the polyhedrin pro-  
79 tein formed by *Bombyx mori*, an insect from the moth family *Bombycidae*. A  
80 cargo protein (i.e., rhBDNF) is co-expressed within the polyhedrin crystal and is  
81 slowly released by breakdown of the PODS® crystals via cell-secreted proteases  
82 (Figure 1B)[9, 18, 22].

83 *2.2. Human pluripotent stem cell culture using dual-compartment microfluidic  
84 device*

85 Human embryonic stem cells (hESCs: H7 and H9, passages number 25–35)  
86 and were obtained from WiCell Research Institute (Madison, Wisconsin, USA).  
87 Human induced pluripotent stem cells (hiPSCs: TC-1133HKK, passage num-  
88 ber 22–35) were generated from human CD34+ cord blood cells using the four  
89 Yamanaka factors at Lonza (Walkersville, Maryland [MD], USA). The hiPSC

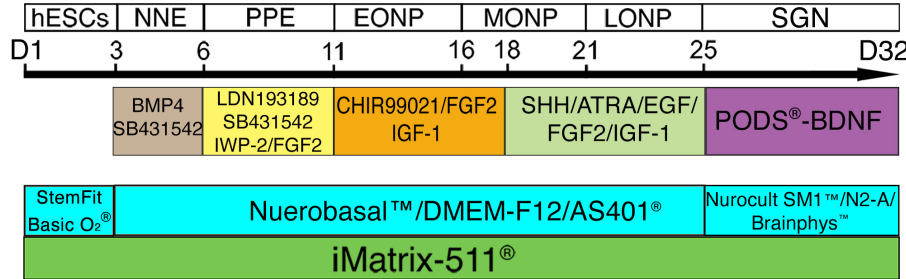


Figure 2: Overview of otic neuronal differentiation protocol for hPSCs. Please see detail in [8, 9, 23, 24] and the Supplemental Data. Each developmental stage is shown at the top, with key treatments shown below. NNE: nonneuronal ectoderm; PPE: preplacodal ectoderm; EONP: early-stage otic neuronal progenitor; MONP: mid-stage otic neuronal progenitor; LONP: late-stage otic neuronal progenitor; BMP4: bone morphogenetic protein 4; SHH: Sonic hedgehog; ATRA: all-trans retinoic acid; EGF: epidermal growth factor; IGF-1: insulin-like growth factor-1; FGF2: fibroblast growth factor 2; N2B27-CDM: chemically defined medium containing N2 and B27 supplements.

90 cell line (TC-1133HKK) was kindly provided by Healios K.K. (Tokyo, Japan).  
 91 hPSC-derived ONPs were derived based on our previously established protocol  
 92 (Supplemental Data) [8, 9, 23, 24]. A step-wise series of ligands and growth  
 93 factors was added to a neuronal induction medium to promote hPSC differen-  
 94 tiation toward the late-stage ONP lineage—mitotic progenitor population that  
 95 generates the SGNs. (Figure 2).

96 Microfluidic devices provide a platform for specifically evaluating axonal re-  
 97 generation [25]. Here, multi-chamber microfluidic devices, Xona™ Microfluidics  
 98 XC150 and XC450 (Xona™ Microfluidics, Research Triangle Park, North Car-  
 99 olina, USA), were used for computational calculation and biological validation  
 100 (Figure 3A–B) of an FEA. The Xona™ device allows for neurites to grow to-  
 101 ward growth factors in the opposite chamber while limiting migration of derived  
 102 ONP cell bodies due to specific dimensions of the device. Additionally, the mi-  
 103 crochannel array between the two chambers mimics the porous bony separation  
 104 (osseous spiral lamina) between the modiolus (where extant SGNs are localized)  
 105 and the scala tympani (where the biohybrid CI will be implanted). Thus the

<sup>106</sup> diffusion profile of the released rhBDNF *in vitro* more accurately predicts that  
<sup>107</sup> of the *in vivo*.

<sup>108</sup> The devices were washed and coated with poly-L-ornithine (PLO, 20 µg/mL  
<sup>109</sup> in H<sub>2</sub>O, Sigma-Aldrich, St. Louis, Missouri [MO], USA) and recombinant  
<sup>110</sup> laminin-511 (iMatrix-511, 0.5 mg/mL, Nacalai USA, San Diego, California [CA],  
<sup>111</sup> USA) according to the manufacturer-outlined protocol. Next, approximately  
<sup>112</sup> 1.75 x 10<sup>5</sup> cells (in 20 µL of media) were added through the top and bottom left  
<sup>113</sup> wells into the somal compartment (i.e., total amount of 3.5 x 10<sup>5</sup> hPSC-derived  
<sup>114</sup> ONPs were added).

<sup>115</sup> PODS®-rhBDNF were placed in the top right well of the neurotrophin com-  
<sup>116</sup> partment (Figure 3A–B) to generate a rhBDNF concentration gradient to pro-  
<sup>117</sup> mote directional neurite growth. hPSC-derived ONPs were cultured for 7 days  
<sup>118</sup> in the Xona™ device to induce otic neuronal differentiation. Note that high-  
<sup>119</sup> density cell cultures were induced to facilitate molecular studies as well as the  
<sup>120</sup> generation of a more biologically relevant neuronal phenotype (i.e., otic lineage)  
<sup>121</sup> [25]. Media was topped off daily after imaging (from 20-40 µL per well).

<sup>122</sup> 2.3. *Enzyme-linked immunosorbent assay for brain-derived neurotrophic factor*

<sup>123</sup> In order to determine the breakdown and release kinetics of PODS®-rhBDNF,  
<sup>124</sup> an experiment measuring rhBDNF concentrations at sequential time points was  
<sup>125</sup> performed. The culture media from both a control and experimental condition  
<sup>126</sup> were collected at each time point and immediately stored at -80°C before run-  
<sup>127</sup> ning an enzyme-linked immunosorbent assay (ELISA) after the final collection.  
<sup>128</sup> The same method was applied to measure the degradation kinetics of rhBDNF  
<sup>129</sup> protein with a carrier protein (Bovine Serum Albumin [BSA]) (#248-BDB-050,  
<sup>130</sup> R&D Systems, Minneapolis, Minnesota, USA). Experimental conditions were  
<sup>131</sup> culture media enriched with 10% fetal bovine serum (FBS) (Thermo Fisher  
<sup>132</sup> Scientific, Waltham, MA, USA). All rhBDNF samples were quantified with a  
<sup>133</sup> BDNF ELISA kit (# BGK23560; PeproTech, Rocky Hill, New Jersey, USA),  
<sup>134</sup> and the results were analyzed with a Synergy HTX Multi-Mode Reader (BioTek,  
<sup>135</sup> Winocski, Vermont, USA) at a 450 nm wavelength, as instructed by the man-

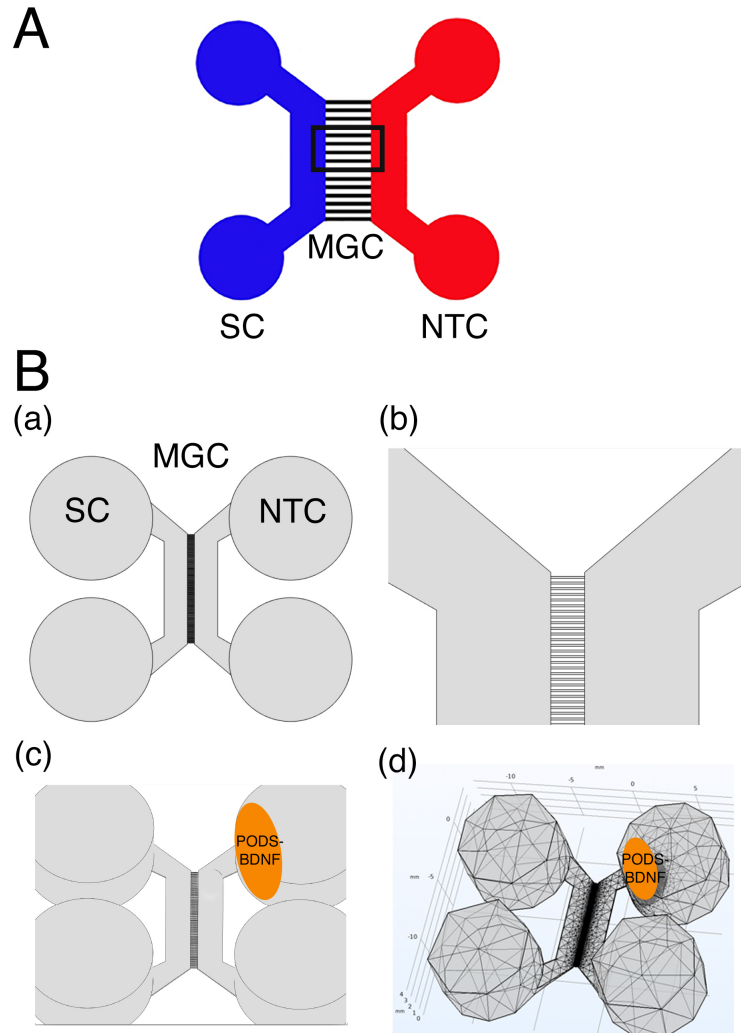


Figure 3: (A): Schematic specification of a Xona™ Microfluidics XC 450. Two main channels (somal compartment (SC) and neurotrophin compartment (NTC)) on either side are connected by a micro-groove channel (MGC) spanning 450  $\mu\text{m}$  with a width of 10  $\mu\text{m}$  (black square). The somal compartment contains hPSC-derived late-stage ONPs (shown in black), while the neurotrophin compartment contains the secreted factors (i.e., BDNF) that are released from PODS®-rhBDNF crystals. (B):(a) Xona™ Microfluidics XC450 device geometry, created at a 1:1 scale with Autodesk Inventor®, in which the diffusion profile of the released BDNF was modeled. (b) Detail of the microchannels adjoining the two compartments of the Xona™ Microfluidics XC450. (c) Xona™ Microfluidics XC450 device showing the optimal area and geometry to localize PODS®-rhBDNF (yellow ellipsoid area). (d): Mesh geometry of the Xona™ XC450 generated with Autodesk Inventor, depicting the localized volume of PODS®-rhBDNF (1  $\mu\text{L}$ ) as an ellipsoid disc.

<sup>136</sup> ufacturer. Molecular kinetics were then calculated using the MATLAB Curve  
<sup>137</sup> Fitting Toolbox (MathWorks, Natick, CA, USA).

<sup>138</sup> *2.4. Sodium dodecyl sulphate-polyacrylamide gel electrophoresis*

<sup>139</sup> Sodium dodecyl-sulfate polyacrylamide gel electrophoresis (SDS-PAGE) is  
<sup>140</sup> commonly used as a method to separate proteins with molecular masses between  
<sup>141</sup> 5 and 250 kDa [26], a range of which is suitable for detecting recombinant hu-  
<sup>142</sup> man BDNF (molecular weight [MW]: 14kDa [27]) and polyhedrin (MW: ~29  
<sup>143</sup> kDa [22]). In this study, SDS-PAGE was used to assess the molar ratio of poly-  
<sup>144</sup> hedrin to BDNF at different quantities. Briefly, each protein sample was diluted  
<sup>145</sup> in deionized water and mixed with 6x Laemmli sample buffer (Bio-Rad Labora-  
<sup>146</sup> tories, Inc., Des Plaines, Illinois [IL], USA) containing 2-mercaptoethanol and  
<sup>147</sup> heated at 100°C for 5 to 20 minutes. Samples were then loaded into precast  
<sup>148</sup> Mini-PROTEAN TGX 4-15% polyacrylamide mini-gels (Bio-Rad Laboratories,  
<sup>149</sup> Inc., Des Plaines, IL, USA). Then, 5 mL of Precision Plus Protein Kaleido-  
<sup>150</sup> scope Prestained Protein Standards (Bio-Rad Laboratories, Inc., Des Plaines,  
<sup>151</sup> IL, USA) were loaded in each gel run. Electrophoresis was performed at room  
<sup>152</sup> temperature for approximately 90 minutes using a constant voltage (100V) in  
<sup>153</sup> 1x solution of Tris-Glycine-SDS electrophoresis buffer (Bio-Rad Laboratories,  
<sup>154</sup> Inc., Des Plaines, IL, USA) until the dye front reached the end of the 60 mm  
<sup>155</sup> gel. After electrophoresis, the mini-gels were rinsed with deionized water 3  
<sup>156</sup> times for 5 minutes and were subsequently incubated in SimplyBlue™ SafeStain  
<sup>157</sup> (ThermoFisher Scientific, Waltham, MA, USA) for one hour at room temper-  
<sup>158</sup> ature with gently agitation. Images obtained from gels were analyzed using  
<sup>159</sup> ImageJ 1.53g (December 4, 2020, the National Institutes of Health, Bethesda,  
<sup>160</sup> MD, USA [28]). The calculated molar ratio was applied to the COMSOL®  
<sup>161</sup> Multiphysics model to accurately predict the amount of rhBDNF released from  
<sup>162</sup> PODS®-rhBDNF. SDS-PAGE was performed according to the manufacturer's  
<sup>163</sup> technical guide (Bio-Rad Laboratories, Inc., Des Plaines, IL, USA).

164     *2.5. Western Blot*

165     The identity of the rhBDNF protein detected by SDS-PAGE was verified  
166     by western blot (Bio-Rad Laboratories, Inc., Des Plaines, IL, USA). Briefly,  
167     the polyvinylidene difluoride (PVDF) membrane was prepared in methanol for  
168     30 seconds before soaking in 1x Tris-Glycine-Methanol transfer buffer for 10  
169     minutes. Wet transfer was performed at 4°C for approximately 60 minutes us-  
170     ing a constant voltage (100V) in 1X solution of Tris-Glycine-Methanol transfer  
171     buffer. After transfer, the membrane was briefly rinsed with 1X Tris-buffered  
172     saline Tween-20 (TBST) and was subsequently blocked in 5% BSA in TBST for  
173     24 hours at 4°C with gentle agitation. The membrane was then rinsed with 1x  
174     TBST before incubating in BDNF polyclonal antibody (ThermoFisher Scien-  
175     tific, Waltham, MA, USA) diluted to 1:1500 in 1% BSA in TBST for 24 hours at  
176     4°C with gentle agitation. Following incubation, the membrane was rinsed in 1x  
177     TBST 5 times for 5 minutes to remove unbound primary antibody. Then, the  
178     membrane was incubated in Goat anti-Rabbit IgG (H+L) horseradish peroxy-  
179     dase (HRP) conjugated secondary antibody (ThermoFisher Scientific, Waltham,  
180     MA, USA) diluted to 1:5000 in 1% BSA in TBST for one hour at room tem-  
181     perature with gentle agitation. Following incubation, the membrane was rinsed  
182     in 1x TBST 5 times for 5 minutes to remove unbound secondary antibody. For  
183     sensitive detection, the membrane was treated with Pierce™ ECL Western Blot-  
184     ting Substrate (ThermoFisher Scientific, Waltham, MA, USA), and visualized  
185     using an Azure 600 Digital Imager (Azure Biosystems, Dublin, CA, USA). Elec-  
186     trophoresis buffer for sample condition and run condition was summarized in  
187     Supplementary Table S1.

188     *2.6. Three-dimensional finite element analysis*

189     We used finite element analysis (FEA) to simulate the BDNF concentration  
190     gradient over time in a multi-chamber microfluidic device. FEA is a compu-  
191     tational numerical technique, which approximates mathematical solutions to  
192     partial differential equations (PDEs) that appropriately simulate complex real-  
193     world problems including stress/strain testing, thermal conduction, and diffu-

194 sion in various geometries and materials. In this study, the FEM allowed us to  
195 predict the concentration gradient with respect to time depending on the num-  
196 ber of PODS®-rhBDNF introduced into the system. To solve the FEM, we used  
197 COMSOL® Multiphysics (version 5.6 [released on November 11, 2020], COM-  
198 SOL, Inc., Burlington, Massachusetts [MA], USA), which is a finite element  
199 method solution tool for engineering and scientific research computations. We  
200 used sustained-release kinetics for PODS®-rhBDNF determined from aforemen-  
201 tioned ELISA studies, SDS-PAGE, as well as data from a previous study from  
202 our group [9]. Device geometry was generated at a 1:1 scale using Autodesk®  
203 Inventor 2019.0.2 (Autodesk, Mill Valley, CA, USA) (Figure 3B). The com-  
204 putational analysis was implemented on a high-performance desktop computer  
205 platform equipped with a 64 GB RAM CPU (AMD Ryzen Threadripper 3990X  
206 64-Core, 128-Thread @ 4.3 GHz) and two GPU cards (NVIDIA GeForce RTX  
207 3080Ti, 12GB 384-bit GFF6X Graphics card).

208 *2.7. Immunocytochemistry and image acquisition*

209 Microfluidic devices were coated with poly-d-lysine (PDL) (#A3890401,  
210 ThermoFisher Scientific, Waltham, MA, USA) and poly-ornithine (PLO) (#  
211 A-004-C, MilliporeSigma, St. Louis, MO, USA) as per the manufacturer's in-  
212 structions. A total of 100,000 dissociated hPSC-derived ONPs were plated into  
213 the somal compartment of the device. On Day 7, 4% (w/v) paraformaldehyde  
214 (PFA) (ThermoFisher Scientific, Waltham, MA, USA) was added to the com-  
215 partments for 20 minutes to fix the cells. ICC was used to stain for GATA3,  
216 PAX8, and beta-III tubulin. These three proteins have shown to appropriately  
217 characterize ONPs in our previous studies [8, 9, 24]. Following PBS wash, cul-  
218 tures were blocked with 5% BSA at room temperature for 1 hour. Cultures  
219 were then incubated overnight at 4°C on a shaker plate in primary antibody  
220 solution using Rabbit anti-Beta-III-Tubulin (1:100, Abcam, Cambridge, MA,  
221 USA), Goat anti-PAX8 (1:500, Abcam, Cambridge, MA, USA), and Mouse  
222 anti-GATA3 (1:500, R&D Systems, Minneapolis, MN, USA). Following PBS  
223 washes, cultures were incubated at room temperature for 90 minutes on a

shaker plate in secondary antibody solution composed of Alexafluor647 anti-Rabbit (1:1000, ThermoFisher Scientific, St. Louis, MO, USA), Alexafluor488 anti-Goat (1:1000, ThermoFisher Scientific, St. Louis, MO, USA), and Alexafluor594 anti-Mouse (1:1000, ThermoFisher Scientific, St. Louis, MO, USA) in 1% BSA. Following PBS -/- washes, cultures were incubated with DAPI for 20 minutes (300 nM, ThermoFisher Scientific, St. Louis, MO, USA). Secondary antibody controls were performed each time multiple primary antibodies were used [29]. Labeling controls (detection controls) were performed for a sample from each batch of hPSC culture [29]. See Supplementary Figure S1 for exemplary figures for these control conditions. Results were imaged using a Nikon Ti2 Widefield Laser Microscope System (Nikon, Tokyo, Japan). Phase-contrast images were captured on a Nikon Eclipse TE2000-U inverted microscope (Nikon, Tokyo, Japan). All fluorescence images were acquired on a Zeiss LSM 510 META laser-scanning confocal microscope (Carl Zeiss, Oberkochen, Germany), a Nikon Ti2 laser scanning confocal microscope (Nikon, Tokyo, Japan), or a Leica SP5 laser-scanning confocal microscope (Leica, Welzlar, Germany). Observers were blinded to the conditions during imaging and tracing. In general, the images were processed with a Image J ver. 1.53j or Matlab R2020b. Further detail on image acquisition and quantification of fluorescent-positive cells can be found in the Supplemental Data.

#### 2.8. Preferred cell orientation analysis

Collective cell migration, where cells organized in a tightly connected fashion migrate as cohesive structures, is a critical biological process to highlight the neurotrophin diffusion profile [30]. To evaluate this process, time-lapse acquisition of images of the Xona™ device was performed using an inverted microscope (Nikon Eclipse TS100, Tokyo, Japan) at Day 1, 3, 5, and 7. Due to the high cell density required for hPSC-ONPs to survive in the somal compartment of the Xona™ device, images were not amenable to manual analysis in most of the cases. To circumvent this problem, we performed a series of image pre-processings that are mainly based on modified binarization-based extraction of

254 alignment score methods with some modifications [31]. We used MATLAB Im-  
255 age Processing Toolbox R2020b (version 9.9.0.1495850, September 30th, 2020,  
256 Mathworks, Natick, MA) for analysis. Please see Supplementary Figure S2 for  
257 further detail. The analysis of directional data in general represents a particular  
258 challenge: there is no reason to designate any particular point on the circle as  
259 zero, and it is somewhat arbitrary depending on where one sets a coordinate  
260 [32, 33]. In this study, we used polar coordinates to determine the directionality  
261 of preferred cell orientation. For this analysis, we again used MATLAB Image  
262 Processing Toolbox R2020b. See detailed discussion on how we determined the  
263 preferred cell orientation in Supplementary Figure S3.

264 *2.9. Neurite alignment vector assay, neurite growth assay and cell migration*  
265 *assay*

266 The microfluidic device allowed us to culture hPSC-derived ONPs in a po-  
267 larized manner and to directly isolate/analyze neurites. To evaluate the neurite  
268 projection into the neurotrophin compartment by derived otic neurons cultured  
269 in the somal compartment, we performed a neurite alignment vector assay. We  
270 also evaluated the length of neurites that grew from hPSC-derived ONPs. For  
271 these purposes, hPSC-derived ONPs were cultured in a Xona™ XC450 for seven  
272 days and then immunostained with *beta*-III tubulin and DAPI. We used two  
273 ImageJ plug-in toolkits, NeuriteTracer and NeuronJ, to assess neurite align-  
274 ment and neurite growth [34, 35]. Due to the bipolar nature of hPSC-derived  
275 ONPs/SGNs, we measured the two longest neurites from the cells [24, 36].  
276 Please see Supplementary Figure S4 for detailed description of this analysis. We  
277 used hPSC-derived ONPs cultured with 800,000 PODS®-rhBDNF as a positive  
278 control. The quantity 800,000 was chosen based on our FEM in that there was  
279 no neurotrophin gradient in the somal compartment. As a negative control, we  
280 used 20 ng/mL of recombinant human BDNF. To evaluate cell migration across  
281 the microgroove channels, we performed cell migration analysis. We manually  
282 counted the number of ONPs that migrated from the somal compartment into  
283 the microchannels and neurotrophin compartment.

284 *2.10. Statistical analysis*

285 When appropriate, and as indicated in each figure, statistical analysis was  
286 performed. Experimental values are typically expressed as mean and standard  
287 error (SE). The majority of the statistical analyses were performed with Python  
288 3.9.6. (Python Software Foundation, Wilmington, Delaware, USA). The follow-  
289 ing libraries were used for the statistical analysis: Scipy, Numpy, Matplotlib,  
290 and Seaborn [37, 38, 39]. Normal distributions were assumed unless mentioned  
291 otherwise. *P* values smaller than 0.05 were considered statistically significant.  
292 For circular statistics, we derived the sample mean vector and its polar coor-  
293 dinate. Mean and confidence intervals were calculated. We chose confidence  
294 coefficient, *Q*, e.g. *Q* = 0.95. To analyze the axial nature of data, especially to  
295 compute the mean vector angle, we doubled each angle and reduced the mul-  
296 tiples modulo 360°. Please see detailed discussion in Supplementary Figure S3  
297 and S5. The Rayleigh test of uniformity and V-test were performed to deter-  
298 mine whether the samples differ significantly from randomness (i.e., where there  
299 is statistical evidence of directionality). One-sample test for the mean angle was  
300 performed to test whether the population mean angle is statistically different  
301 from the given angle. In all of our circular statistics, von Mises distribution was  
302 assumed and also verified. Circular statistics were performed using CircStat: A  
303 MATLAB Toolbox [33, 40]. Please see detailed description of circular statistics  
304 in Supplementary Figure S3 and S5. Experiments were done in three biological  
305 replicates unless otherwise specified in Figure captions.

306 **3. Results**

The appropriate number of PODS®-rhBDNF crystals to induce an effective neurotrophin gradient for otic neuronal differentiation and directed neurite outgrowth was calculated using a three-dimensional FEA that predicts the concentration profile of BDNF formed through the gradual release and diffusion of BDNF from PODS®-rhBDNF. First, we quantified the chemical kinetics of this phenomenon with ELISA testing (Figure 4) to establish the parameters for

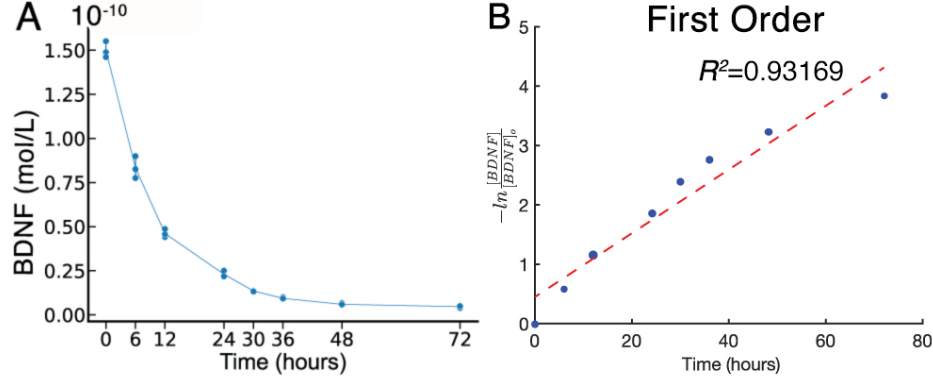
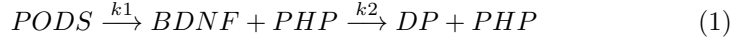


Figure 4: Chemical kinetics of Brain Derived Neurotrophic Factor (BDNF). (A): Concentration of rhBDNF in solution over 72 hours after initial application. (B):  $\frac{1}{[BDNF]}$  data fit to first order curve. Please see other curve fit data in Supplemental Figure 1. Red line: fitted curve, blue dots: individual data point.  $k_2$  is defined as slope of fitted curve.

the FEA. Here, two consecutive chemical reactions occur: 1) the breakdown of PODS® crystals into polyhedrin protein and rhBDNF, and 2) the degradation of rhBDNF toward the degradation product (Equation (1)).



where  $DP$  is the degradation product of the released rhBDNF, PHP is the polyhedrin protein, and  $k_1$  and  $k_2$  are the rate constants ( $\frac{1}{\text{hour}}$ ) for their respective reactions.

Degradation kinetics data for rhBDNF was collected while monitoring rhBDNF concentration after introducing a predefined amount into a single well of solution. The data obtained throughout the first 72 hours indicate an exponential decay, suggesting first order kinetics (Figure 4). To confirm this notion, we performed a linear and nonlinear least square analysis of the kinetic data with the MATLAB Curve Fitting Toolbox. We found that the corresponding  $R^2$  was 0.93169 for the first order curve-fit, confirming that the degradation kinetics was indeed first order. The rate constant for a first order reaction is defined to be slope of the time plot of the logarithmic ratio between concentration and

319 initial concentration. The value for  $k_2$  ( $0.0679 (\frac{1}{hour})$ ) is the slope of the loga-  
320 rithm of the ratio between concentration and initial concentration (See further  
321 detail in Supplementary Figure S7). Furthermore, data for the complete chemi-  
322 cal reaction were collected by similarly monitoring rhBDNF concentration over  
323 time after placing a predefined amount of PODS®-rhBDNF into a single well  
324 of solution. The data collected appeared to fit the curve for Equation 2, which  
325 describes the concentration of the intermediate product of two consecutive first  
326 order reactions:

$$C_{rhBDNF} = C_{PODS} \cdot k_1 \cdot \left( \frac{e^{-k_1 \cdot t}}{k_2 - k_1} + \frac{e^{-k_2 \cdot t}}{k_1 - k_2} \right) \quad (2)$$

327 where  $C_{rhBDNF}$  is the concentration of rhBDNF and  $C_{PODS}$  is the concentra-  
328 tion of PODS® [43].

329 We successfully fit the data to this equation's respective curve and empiri-  
330 cally approximated  $k_1$  to be  $0.00686 (\frac{1}{hour})$  after plugging in our value for  $k_2$   
331 (See further detail in Supplementary Figure S7).

332 SDS-PAGE was used to separate PODS®-rhBDNF crystals into its con-  
333 stituent proteins to determine the molar ratio of polyhedrin to rhBDNF. Vi-  
334 sualization with Coomassie G-250 solution (Figure 6A) revealed three distinct  
335 protein bands at 18.8 (a), 28.0 (b), and 46.8 (c) kDa, which correspond with  
336 the molecular weights of H1-tagged BDNF monomer, polyhedrin, and H1-tagged  
337 BDNF monomer attached with polyhedrin, respectively. Western blot analy-  
338 sis was subsequently conducted to confirm the identity of the 18.8 kDa band  
339 as rhBDNF. Enhanced chemiluminescence (Figure 6B) revealed four protein  
340 bands at 14.0 (a), 18.8 (b), 37.6 (c), and 46.8 (d) kDa, which correspond with  
341 the molecular weights of rhBDNF monomer, H1-tagged BDNF monomer, H1-  
342 tagged BDNF dimer, and H1-tagged BDNF monomer attached with polyhedrin.  
343 Immunoblot detection of the 18.8 kDa band further implicates its identity as  
344 rhBDNF. SDS-PAGE images were converted to 8-bit grayscale and mean cor-  
345 rected integrated pixel intensity values were calculated for protein bands located  
346 at 28.0 and 18.8 kDa; the protein band detected at 46.8 kDa was omitted from

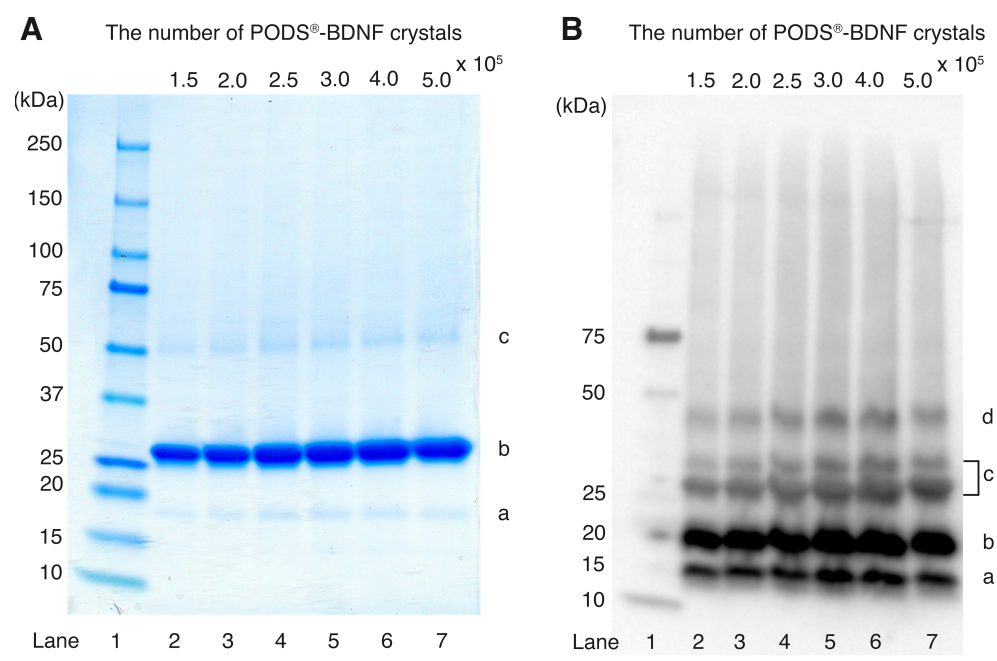
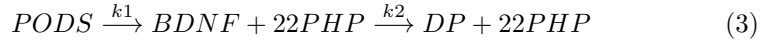


Figure 5: (A): SDS-PAGE analysis of PODS®-rhBDNF. Samples containing six quantities of PODS®-rhBDNF crystals were run on precast 4-15% polyacrylamide mini-gels and stained with Coomassie G-250 solution for visualization. Protein bands appear at approximately 18.8 (a), 28.0 (b), and 46.8 kDa (c). Lane 1: molecular weight marker. Lanes 2-7: samples containing

<sup>347</sup> the final computation based on the fact that it contained a 1:1 ratio of poly-  
<sup>348</sup> hedrin to BDNF. Results indicate that the molecular ratio of polyhedrin to  
<sup>349</sup> rhBDNF is approximately 22:1. This transforms Equation (1) into:



<sup>350</sup> Using these calculated rate constants with the calculated molar ratio, the  
<sup>351</sup> resulting chemical gradient over time after PODS®-rhBDNF placement can be  
<sup>352</sup> solved for any geometry by applying Fick's second Law of diffusion (Equation  
<sup>353</sup> 4) and the appropriate boundary (Equations 5 and 6) and initial conditions  
<sup>354</sup> (Equation 7):

$$\frac{dC}{dt} = \nabla \cdot (\nabla C \cdot D) - k_2 \cdot C \quad (4)$$

<sup>355</sup> Boundary Conditions:

$$\delta C \Big|_{walls} = 0 \quad (5)$$

<sup>356</sup> and

$$\delta C \Big|_{PODS} = k_1 \cdot PODS_0 \cdot e^{-k_1 \cdot t} \quad (6)$$

Initial conditions:

$$C \Big|_{t=0} = 0 \quad (7)$$

<sup>357</sup> where  $C$  is the concentration of rhBDNF,  $D$  is diffusivity of rhBDNF (6.76  
<sup>358</sup>  $\frac{mm^2}{day}$  [44]),  $-k_2 \cdot C$  is the sink term corresponding to the degradation and cell-  
<sup>359</sup> utilization of the rhBDNF, and  $PODS_0$  is the initial concentration of the cargo  
<sup>360</sup> protein (i.e., BDNF) within the PODS® crystals. The first boundary condition  
<sup>361</sup> (Equation 4) shows that the concentrations of rhBDNF at the walls of the  
<sup>362</sup> microfluidic device are fixed at 0. The second boundary condition (Equation 5)  
<sup>363</sup> represents the exponential nature of the decay of PODS®. Note that both are  
<sup>364</sup> Neumann boundary conditions.

365 We empirically tested two available microchannel lengths—(i.e., Xona<sup>TM</sup>-  
366 XC150 [150  $\mu\text{m}$ ] and Xona<sup>TM</sup>-XC450 [450  $\mu\text{m}$ ]). This was done first because  
367 mass (i.e., BDNF) transport from the neurotrophin compartment through the  
368 micro-groove channels into the somal compartment is an important factor in  
369 generating the concentration gradient *via* diffusion mixing. We determined that  
370 the Xona<sup>TM</sup> Microfluidics XC450 was more appropriate for this study as the XC-  
371 150's micro-groove channels were not long enough to generate the appropriate  
372 concentration gradient throughout the somal compartment. This feature is rel-  
373 evant to human inner ear because the micro-groove channels in the Xona device  
374 simulates the presence of the osseous spiral lamina and modiolus between the  
375 scala tympani and SGNs [41, 42]. Following device selection, we generated a  
376 three-dimensional geometry mesh of the XC450 for the FEA (Figure 3B(d)).  
377 Please see Supplementary Figure S6 for detailed measurements of the mesh.

378 The finite element model was then computed for different PODS<sup>®</sup>-rhBDNF  
379 concentrations and time intervals to empirically optimize the rhBDNF concen-  
380 tration gradient for hPSC-derived ONP differentiation into SGNs as well as  
381 directed neurite extension. Figure 6 shows FEM-computed rhBDNF concen-  
382 tration gradients for 20,000 PODS<sup>®</sup>-rhBDNF from Day 1–7. Note that the  
383 rhBDNF concentrations were greater throughout D2–5 to promote the neuronal  
384 differentiation and neurite outgrowth observed on D7 (Figure 6B). Computed  
385 diffusion flux was uniform throughout D1–7 (Figure 6C). Also note that highest  
386 concentration of rhBDNF released from PODS<sup>®</sup>-crystals was greater than 50  
387 pg/mL, the concentration sufficient for otic neuronal differentiation and neurite  
388 outgrowth of hPSC-derived ONP 3D spheroids determined in our previously  
389 published data [9]. Optimization of the adequate number of PODS<sup>®</sup>-rhBDNF  
390 was performed empirically; we also performed FEA with 10,000 and 40,000  
391 PODS<sup>®</sup>-rhBDNF. Please see detailed discussion for the empirical optimization  
392 in Supplementary Figure S8.

393 To objectively compare the degree of otic neuronal differentiation in the  
394 hPSC-derived ONPs, we performed quantitative analysis of PAX8 and GATA3  
395 double-positive cells using immunocytochemistry. We chose PAX8 and GATA3

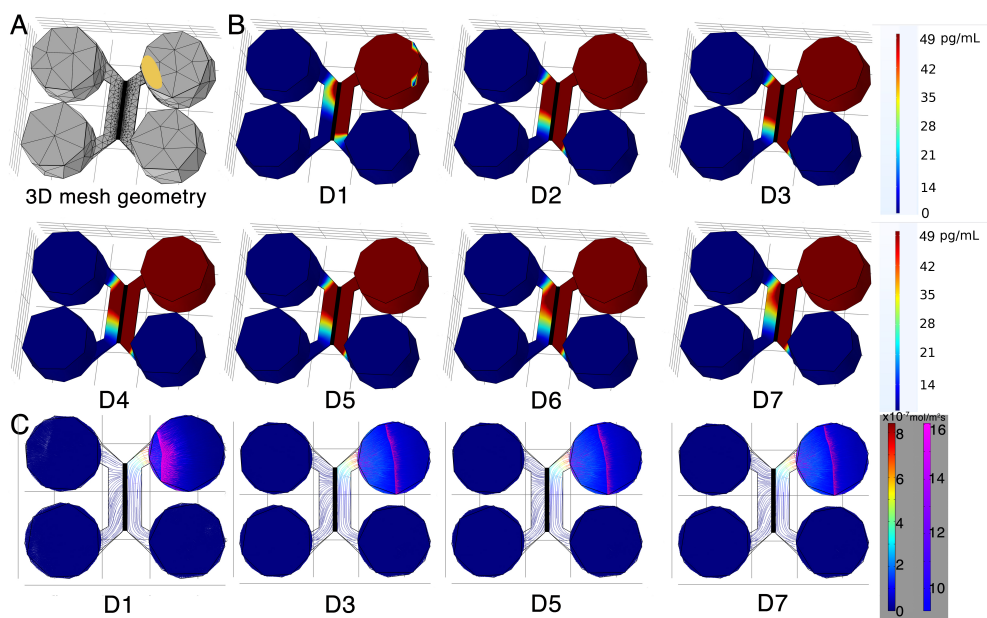


Figure 6: (A): 3D mesh geometry of a Xona™ XC450 created with Autodesk Inventor. A PODS®-rhBDNF ellipsoid disc is shown in yellow. (B): rhBDNF concentration gradient for 20,000 PODS®-rhBDNF from D1–D7. Note that the model does not account for media changes during the culture period. The corresponding color map shown has a range from 0 ng/mL to 49 pg/mL. (C): Diffusion flux ( $\text{mol}/\text{m}^2\text{s}$ ) was computed using COMSOL Chemical Engineering module on D1, D3, D5, and D7.

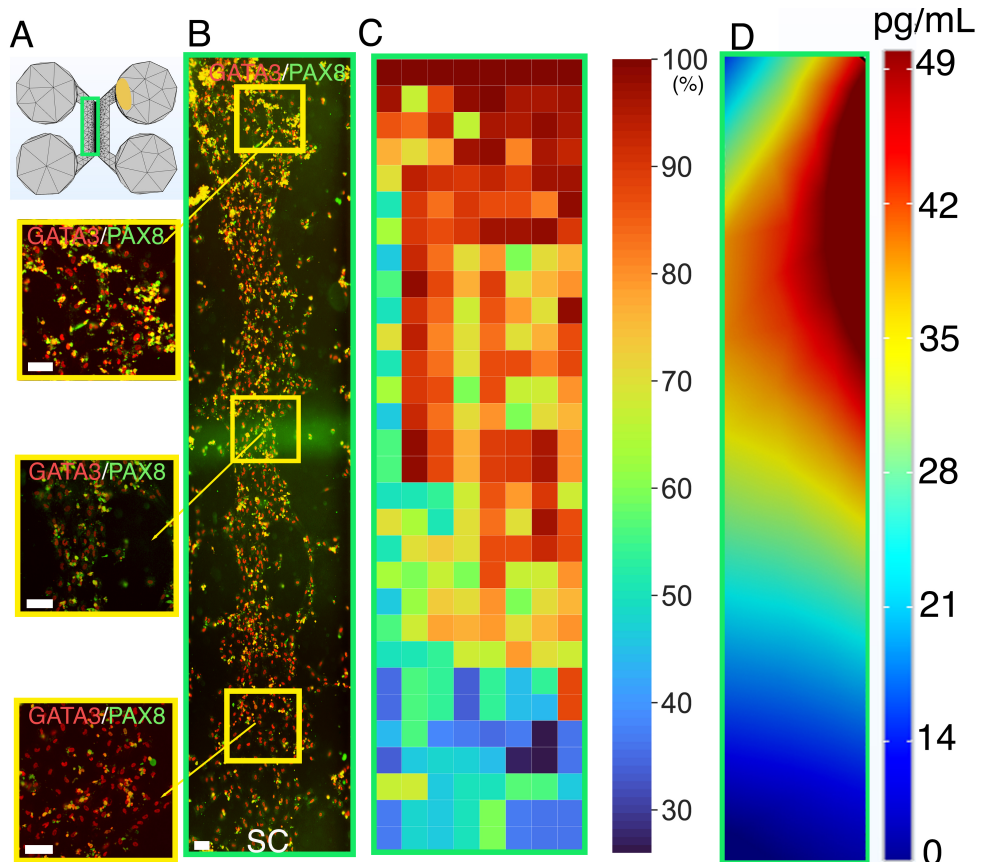


Figure 7: Human PSC-derived late-stage ONPs grown in a microfluidic device at Day 7 were stained for GATA3 (red) and PAX8 (green). (A): Geometry mesh of the microfluidic device Xona™ XC450 generated by Autodesk Inventor. The green square indicates the cell seeding location in the somal compartment of the device. An ellipsoid PODS®-rhBDNF disc is shown in yellow. (B): Cells were analyzed by staining with neuronal markers GATA3 (red) and PAX8 (green). Yellow highlighted regions are magnified on the left. SC: somal compartment. (C): Heat-map representation of double-positivity of hPSC-derived ONPs in the device for GATA3 and PAX8 ( $n = 3$ ). Double-positivity increases from the lower to the upper portion of the somal compartment, suggesting that the higher BDNF concentration in the upper portion of the device improves differentiation. Scale bar:  $100 \mu\text{m}$ . (D): Prediction of BDNF concentration gradient released from PODS®-rhBDNF at seven days in culture using the finite element model. The corresponding color map is shown with a range from 0–49 pg/mL.

for this analysis because our previous studies indicated high expression of these protein markers in late-stage ONPs and early-stage SGNs [8, 9, 24]. Cells were stained in the somal compartment of the Xona™ device, highlighted in green in Figure 7A. Figure 7B shows the resulting image of cells in the somal compartment, and a heat-map representation of the percentage of double-positive cells is shown in Figure 7C. It should be noted here that the heat-map is sensitive to the differences in cell density across channel. This was accounted by averaging the double-positivity across three biological replicates. The heat-map indicates higher double-positivity in the upper region of the somal compartment, which is closest to the PODS®-rhBDNF disc placement (shown as an orange ellipse in Figure 7A) in the neurotrophin compartment. Double-positivity decreases in the somal compartment as distance from the PODS®-rhBDNF disc increases, supporting the presence of a rhBDNF neurotrophin gradient as predicted by our computational model (Figure 7D).

We defined two hypothetical directional angles to predict the orientation of hPSC-derived ONPs and neurite growth (Figure 8). The  $n$ -dimensional Euclidean space, denoted by  $\mathbb{R}^n$ , is a linear vector space in that we can use polar coordinates to compute the directionality of cells and neurites [45]. Here, we used  $n = 1$  and  $2$ . For one-dimensional Euclidean space ( $n = 1$ ), we simply drew a line for the Euclidean distance—the shortest distance between two points as shown in Figure 8A(b) (dark green lines). The two points were 1) the center point of the PODS®-rhBDNF disc ( $P$ ) and 2) the mid point of the medial side ( $Q_{1-5}$ ) (i.e., the near side to microgroove channels) of a pre-designated square (shown as a black square, zones 1–5 in Figure 8), respectively. The Euclidean distance angle (EDA),  $\phi_i$ , was defined as the angle between the horizontal line zero direction and the line  $PQ_i$  that consists of the Euclidean distance where  $i = 1 - 5$ .

For two-dimensional Euclidean space ( $n = 2$ ), we utilized Fick's first law, which dictates that the diffusion flux ( $D$ ) is proportional to the concentration gradient ( $C$ ) [46]. Based on this theorem, the direction of a flow vector can be used to represent the concentration gradient for directionality. We hypothesized

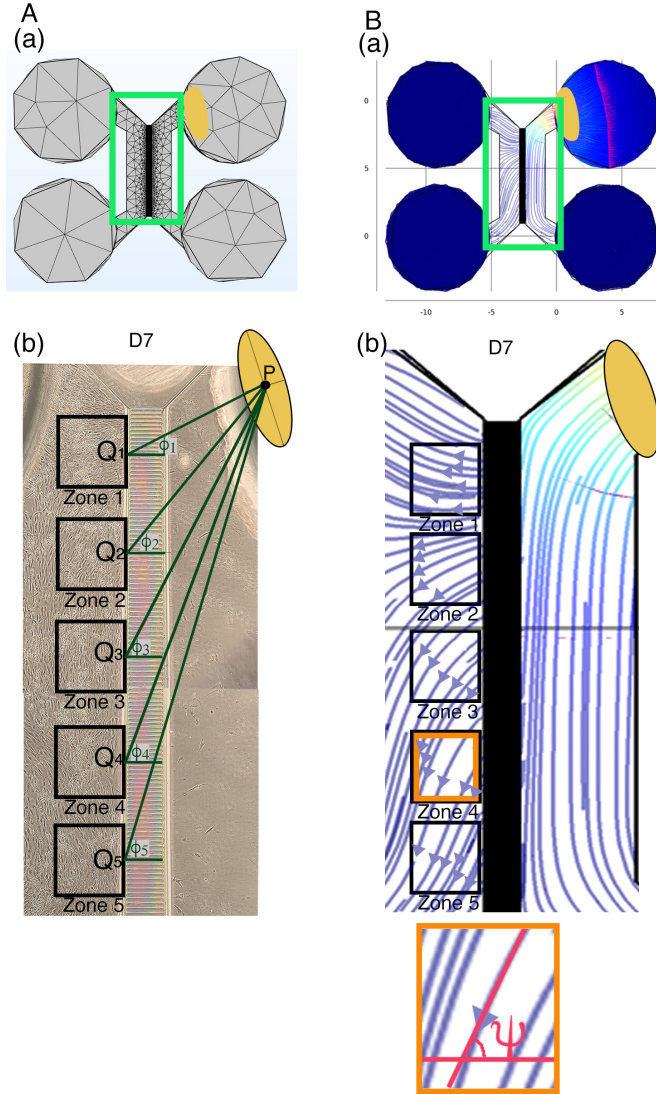


Figure 8: (A): Defining the Euclidean distance angle (EDA). (a) X-Y plane geometry mesh of a Xona™ XC450 device. Green square shows the area corresponding to the phase-contrast image below. An ellipsoid PODS®-rhBDNF disc is shown in yellow. (b) Yellow ellipse once again indicates the location of a disc containing PODS®-rhBDNF crystals (P: the center of this ellipse). In the somal compartment of the Xona™ XC450 device, we defined Zone 1–5, shown in black squares. A line was drawn from the center of the PODS®-rhBDNF disc (P) to ( $Q_1$ – $Q_5$ ) (i.e., the near side to microgroove channels) of a pre-designated square (shown as a black square, zone 1–5) [i.e.,zone 1–5]). The Euclidean distance angle (EDA) for zone 1–5 was defined as  $\phi_i$ ,  $i = 1–5$ . (B): Defining diffusion flux angle (DFA). (a) Diffusion flux in the Xona™ XC450. Green squared area shows somal and neurotrophin compartments, which are magnified in (b). (b) Magnified image of diffusion flux of Zone 1–5 in the Xona™ XC450. Orange highlighted zone (zone 4) was highlighted at the bottom of (b), defining the DFA ( $\psi$ ).

here that cell orientation is directionally controlled by the flux vector which is driven by the concentration gradient. Figure 8B shows the flow vectors in the somal compartment at Day 7 computed by the COMSOL Chemical Reaction Engineering module. We averaged the 10 flow vectors in each of five zones in Figure 8 to compute the diffusion flux angle (DFA),  $\psi_i$ , where  $i = 1\text{--}5$  in Figure 8. To lighten the computational intensity, we reduced the dimension from 3D to 2D to compute diffusion flux. Please see justification in Supplementary Data. All of the computed EDAs and DFAs can be found in Supplementary Table 2.

Figure 9 shows time-series of microscopic phase-contrast photomicrographs obtained on Day 1, 3, and 7 in the five zones in the Xona™ XC450. Each preferred orientation of any given cell was computed and then plotted on a polar diagram (blue circle). Mean vector angle (MVA, shown in red line on Figure 9) and median vector angle were computed. All of the polar diagrams in Figure 9 show that preferred orientation of hPSC-derived ONPs distribute in an unimodal distribution. We also confirmed that a von Mises distribution is appropriate for these sets of data (See Supplementary Figure S9). We, therefore, then tested further to see if the cells had tendency to be oriented to a certain direction. To test this hypothesis, we used the Rayleigh test of uniformity to evaluate whether there is statistical evidence of circular directionality [32]. Computed  $p$  values for all the 15 conditions were less than 0.05, demonstrating that all of the conditions had statistically significant directionality. To further validate whether the observed angles have a tendency to cluster around the two hypothetical angles (i.e., EDA and DFA), we then performed the V test. Once again,  $p$  values for all 15 conditions were less than 0.05 except one (Zone 5 on Day 1), re-demonstrating that most of the conditions had statistically significant tendencies to cluster around the EDAs and DFAs. Additionally, we performed one sample test for the mean vector angle, which is similar to a one sample t-test on a linear scale. There was only one condition (Zone 1, day 1) that was statistically significant for EDA, whereas most of the conditions on Day 3 and 7 were statistically significant for DFA. Therefore, our results here demonstrated that hPSC-derived ONPs had greater tendency to cluster around DFA than

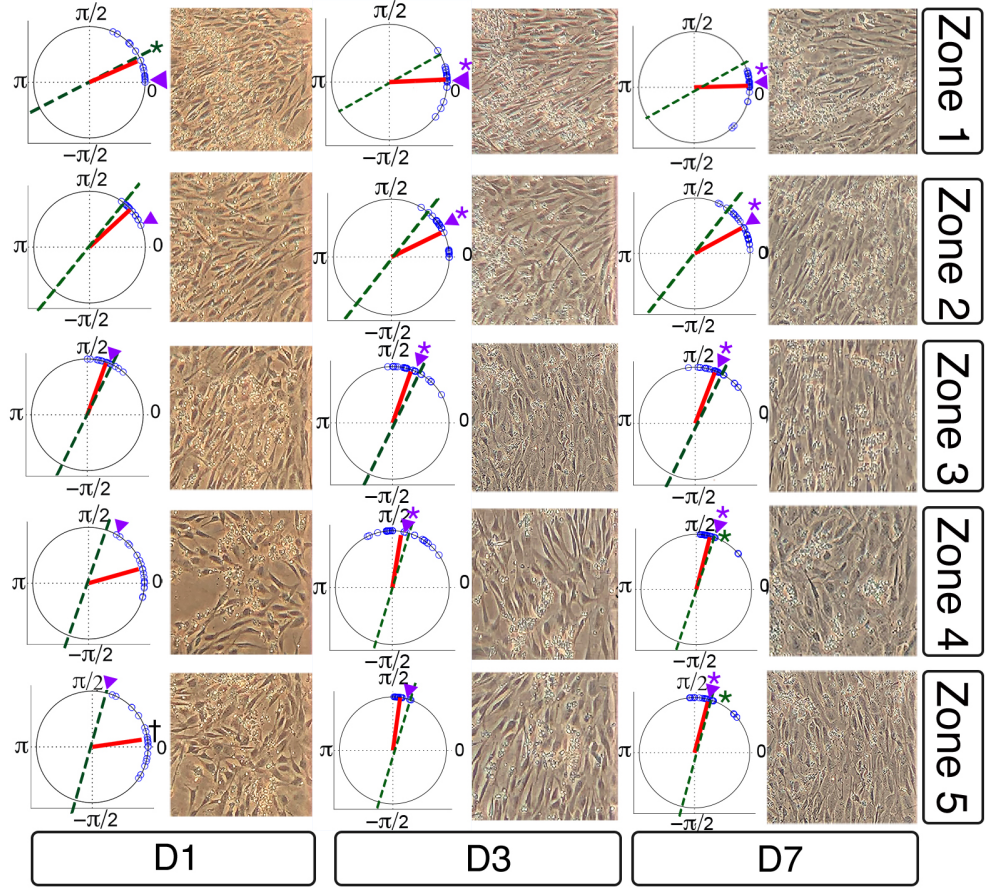


Figure 9: Preferred cell orientation analysis. Sequential phase-contrast images of the somal compartment of the Xona™ XC450 device in zones 1–5 (see Figure 8) on day 1 (D1), day 3 (D3), and day 7 (D7). A corresponding polar histogram indicates preferred orientation of hPSC-derived ONPs in an angle ( $0$ – $2\pi$  radians) in blue circles. Mean vector angle is shown in red line. Green dotted line shows Euclidean Distance Angle (EDA) and purple triangle indicates Diffusion Flow Angle (DFA). † symbol indicates that  $p$  value  $> 0.01$ . \* symbol indicates that the mean vector angle fits within the 95% confidence internal ( $\alpha < 0.05$ ).

458 EDA. All computed statistical values are shown in Supplementary Table S2.

459 To evaluate the direction of neurites of hPSC-derived ONPs, we first de-  
460 fined EDA in Region 1-3 ( $\phi'_j$ ,  $j = 1 - 3$ ) (Figure 10A) and DFA ( $\psi'_j$ ,  $j = 1 - 3$ );  
461 similarly defined  $\phi_i$  and  $\psi_i$  as in Figure 8. All of the EDAs and DFAs defined  
462 here can be found in Supplementary Table S3. Polar histograms of the neurite  
463 direction angle in Regions 1–3 indicated that the two longest neurites were bi-  
464 modal in nature (Figure 10B). In contrast, polar histograms of those cultured  
465 with rhBDNF (negative control) and 800,000 PODS®-BNDF (positive control)  
466 did not indicate bimodal distribution—the neurites did not show directionality  
467 (Figure 10C). The Rayleigh test of uniformity for both the positive and negative  
468 control were greater than 0.05, demonstrating that both of the conditions had  
469 no statistically significant directionality (Supplementary Table S3: highlighted  
470 in green). We also analyzed the direction of the neurites using circular statistics.  
471 To obtain more realistic mean vector angles, we doubled each angle and reduced  
472 the multiples modulo 360°. In circular statistics, the bimodal distributed data  
473 can be transformed into a unimodal data by doubling the angle [32]. The mean  
474 vector angles in Figure 10D (right column) indicates the situation where the  
475 vectors were canceled out between the two groups of angles distributed in a bi-  
476 modal fashion, resulting in inaccurate representation. A circular plot in Figure  
477 10D (right column) showed doubled angles, representing actual representation  
478 of the neurite vector angles. In all of the three regions, the Reyleigh test and V  
479 test for EDA and DFA indicated directionality (Supplementary Table S3). One  
480 sample test for the mean vector angles in Region 1–3 indicated that they were  
481 not statistically different from DFA, but all of the three mean vector angles were  
482 statistically different from EDA.

483 We also stained the devices for  $\beta$ -III tubulin to track neurite growth and  
484 extension across the micro-groove channels as well as cell migration in three  
485 selected regions (Figure 10A). The location of the PODS®-rhBDNF disc in  
486 relation to the regions of interest in Figure 11A is indicated by a yellow cir-  
487 cle. Quantitative analyses were performed and summarized in Figure 11B. Our  
488 data indicate that neurite length is dependent on rhBDNF concentration, with

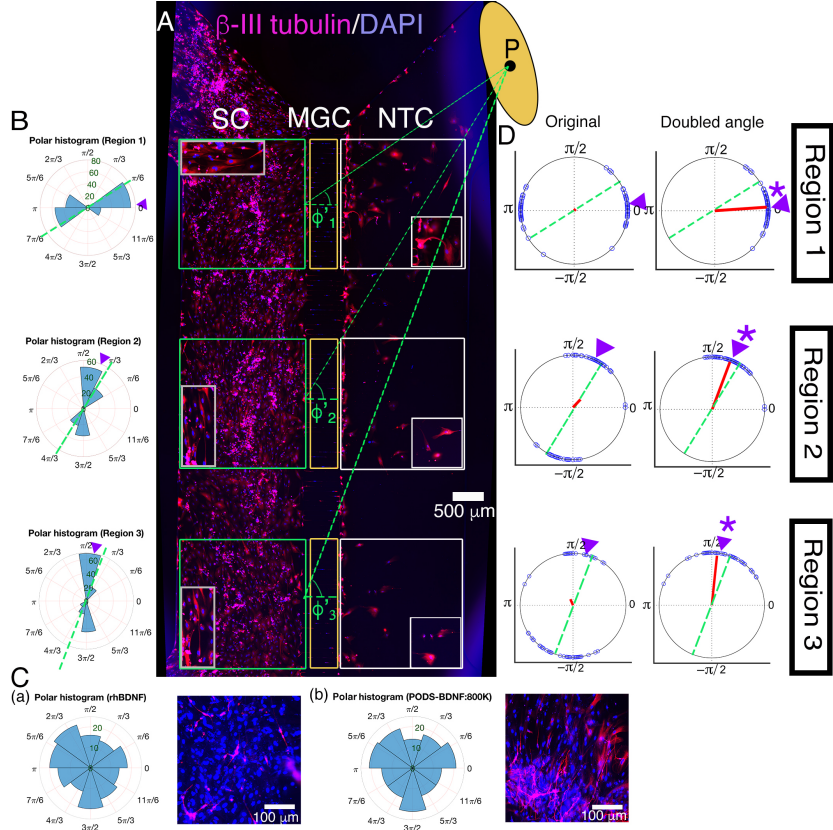


Figure 10: (A): Immunohistochemistry of hPSC-derived ONPs cultured in the Xona™ XC450 for seven days with  $\beta$ -III-Tubulin (pink fluorescence) and DAPI (blue fluorescence). A green line was drawn from the center of the BDNF disc (P) to the mid point of each of three pre-determined squares (Regions 1–3) in the somal compartment to define Euclidean Distance Angle (EDA:  $\phi_i^i$ ,  $i = 1 - 3$ ). Green square: somal compartment (SC); yellow square: microgroove channels (MGC); white square: Neurotrophin compartment (NTC). High-power magnified images of the NTC and SC are shown. An ellipsoid PODS®-rhBDNF disc is shown in yellow. P: the center of the disc. (B): Polar histogram of neurite directional angles of hPSC-derived ONPs in the Xona™ XC450 at Day 7 (D7). The two longest neurites were measured. EDA: green dotted line. DFA: purple triangle. (C): (a) Right: Polar histogram of neurite directional angles of hPSC-derived ONPs cultured with 20 ng/mL of recombinant human BDNF for seven days. Left: Corresponding photomicrograph of immunocytochemistry with  $\beta$ -III tubulin (pink) and DAPI (blue). (b) Right: Polar histogram of neurite directional angles of hPSC-derived ONPs cultured with 800,000 of PODS®-rhBDNF for seven days. Left: Corresponding photomicrograph of immunocytochemistry with  $\beta$ -III tubulin (pink) and DAPI (blue). (D): A circular plot of neurite directional angle of hPSC-derived ONPs in Region 1–3. Once again, the two longest neurites were plotted on a unit circle. Right column: Original directional angle distribution. Left column: the method of doubling the angle applied to the original data. Each datum point is shown as a blue circle. Mean vector angle is shown as a red line. Green dotted line shows Euclidean Distance Angle (EDA) and purple triangle indicates Diffusion Flow Angle (DFA). \* symbol indicates that the mean vector angle fits within the 95% confidence internal ( $\alpha < 0.05$ .)

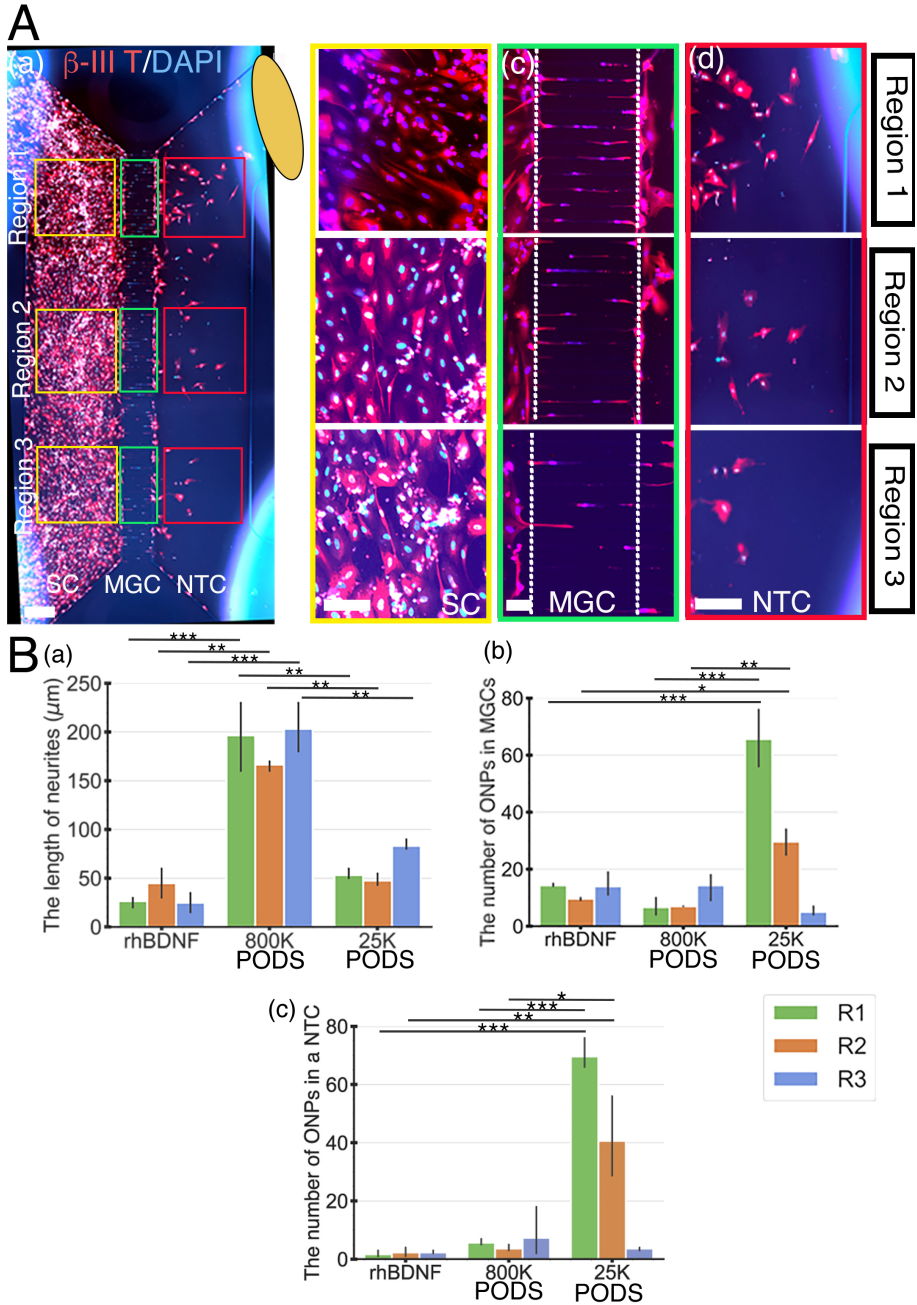


Figure 11: Human PSC-derived late-stage ONPs in the microfluidic device were stained with  $\beta$ -III tubulin (red) and DAPI (blue) to measure cell migration. (A): Late-stage ONPs stained after seven days in culture (a) with regions highlighted and magnified in the somal compartment (b), microgroove channels (c), and neurotrophin compartment (d). SC: somal compartment, MGC: microgroove channels, NTC: neurotrophic compartment. An ellipse-shaped PODS®-rhBDNF disc is shown in yellow. Scale bar (a): 500  $\mu\text{m}$ ; (b)–(d): 100  $\mu\text{m}$ . (B): Quantitative analyses of cell migration and neurite extension in devices using recombinant human BDNF, 800,000 PODS®-rhBDNF, or 20,000 PODS®-rhBDNF. \* :  $p < 0.05$ , \*\*:  $p < 0.01$ , \*\*\*:  $p < 0.001$ .

489 greater amounts of PODS<sup>®</sup>-rhBDNF promoting longer neurite growth (Figure  
490 11B(a)). Lesser amounts of PODS<sup>®</sup>-rhBDNF, however, are necessary to cre-  
491 ate an appropriate concentration gradient. In the presence of 20,000 PODS<sup>®</sup>-  
492 rhBDNF, both neurite extension into the microchannels and cell migration into  
493 the neurotrophin compartment are greatest in the region closest to the BDNF  
494 source and decrease further from the PODS<sup>®</sup>-rhBDNF (Figure 11B(b,c)). Cell  
495 migration is dependent on the distance from the source of BDNF, thus suggest-  
496 ing the presence of a BDNF gradient as predicted by our model. Note that the  
497 Xona microchannels intended to prevent from migration across channels.

498 **4. Discussion**

499 *4.1. Challenges of neurotrophin treatment in the inner ear*

500 This is a proof-of-concept study for the realization of a neurotrophic strip  
501 to ascertain its scientific/technological parameters in a controlled *in vitro* en-  
502 vironment. Neurotrophin gradients have been studied in multiple contexts  
503 [47, 48, 49]. However, it has not been feasible to reliably provide, and maintain,  
504 such a gradient to neurons *in vivo*, primarily because of challenges including  
505 failure to provide a sustainable source. Furthermore, while neurotrophin treat-  
506 ment has been recognized as a potential treatment for sensorineural hearing loss,  
507 there has not been long-term clinical success in this avenue to date. Most recent  
508 relevant clinical trials used adeno-associated virus (AAV2) to deliver BDNF to  
509 the brain [50]. Although compelling, this treatment does not attempt to pre-  
510 cisely control the concentration of BDNF, which could potentially interfere with  
511 normal functions in the target organ [51]. Furthermore, this treatment may not  
512 be applicable to the inner ear, as the procedure is MR-guided-infeasible in the  
513 inner ear. In this study, we used PODS<sup>®</sup>-rhBDNF to generate and maintain a  
514 neurotrophic gradient in a controlled manner. Our results indicate that 20,000  
515 PODS-rhBDNF allowed for a rhBDNF neurotrophin gradient such that hESC-  
516 derived ONPs survived, differentiated toward human SGNs, and also established  
517 directional neurite outgrowth in a microfluidic device. Furthermore, our pro-

posed solution has greater potential to be translated into clinical practice; in addition to its proven natural self-sustainability, we have previously shown that transplantation of PODS-rhBDNF is met with little immune rejection when embedded in a nanofibrillar cellulose hydrogel in mice [9].

#### 4.2. Microfluidic device-generated gradient

We used a microfluidic device to advance our understanding of directional neurite growth and otic neuronal differentiation in response to a rhBDNF concentration gradient [52]. Among many *in vitro* concentration gradient sustaining culture devices, microfluidic devices have overcome many of the deficits that conventional platforms (i.e., the Boyden chamber, Dunn chambers, or compartmentalized diffusion chambers) face [52]. Conventional platforms tend to be sub-optimal in manipulating small volumes of fluid at the order of microliters. Growth factors and proteins are used in minute amounts in our microfluidic device, and cultured stem cells are able to interact with endogenous factors at biologically relevant concentrations. As mentioned earlier, this micro-environment more accurately represents *in vivo* conditions. The Xona™ device can be used to create and sustain a three-dimensional concentration gradient over time (duration dependent on the half-life of the molecule) because of its microchannel array. The device limits convective flow in the gradient-forming areas by introducing microgroove channels that generate high fluidic resistance, thereby limiting flow to diffusion. The high resistance of the microchannel array also prolongs diffusion across them, thereby increasing gradient formation decreasing gradient steepness, essentially elongating it. These features motivated us to generate a FEM, which predicted the rhBDNF gradients associated with different numbers of PODS®-BDNF crystals. Note, however, that this environment is geometrically different from the micro-environment in the inner ear—a mesh geometry of the cochlea will be needed to compute the PODS®-BDNF crystal number for the next step of this study.

546     *4.3. BDNF and polyhedrin protein*

547     Over the course of past 20–30 years, it has been established that BDNF  
548     mediates survival and differentiation activities of SGNs by binding and activating  
549     tyrosine kinase receptor kinase B (TrkB), a member of the larger family of  
550     Trk receptors [20]. Numerous studies have reported that BDNF can palliate  
551     SGN degeneration in ototoxically deafened animals, a widely accepted model  
552     for retrograde trans-synaptic SGN degeneration secondary to hair cell destruc-  
553     tion [13, 14, 53, 54]. Additionally, it has been confirmed that there is a positive  
554     correlation between SGN counts and CI performance [55]. It is then safe to  
555     presume that treating CI recipients with BDNF would enhance overall CI per-  
556     formance, by preserving SGNs and their neurites. However, simply introducing  
557     BDNF into the inner ear poses significant hurdles. Although promising, BDNF  
558     treatment in humans has not been implemented in the inner ear.

559     Unsuccessful BDNF treatment can be explained by several factors [56]. The  
560     blood half-life of BDNF protein is extremely short: only 1–10 minutes in plasma  
561     [57, 58] and one hour in CSF [59]. BDNF’s high degradation rate would require  
562     continuous replenishment, impractical in the clinical setting. Furthermore, in-  
563     troduction of BDNF in solution would promote non-directional neurite growth  
564     where directed neurite growth is essential—especially in the case of our proposed  
565     new-generation bioactive CI. Directing neurite growth towards the CI electrode  
566     array is pivotal in the ultimate goal of enhancing performance through the  
567     narrowing of the electrode-neuron gap. The PODS® system precludes the phe-  
568     nomena by its localized, gradual release of growth factor. The steady supply  
569     of BDNF from a localized origin not only creates a concentration gradient, but  
570     maintains it over time. As seen in Figures 4–6, we were able to perform a finite  
571     element analysis based on data we collected describing the chemical release ki-  
572     netics and molar ratio of PODS®-BDNF system. It is clearly visible that the  
573     slow-release nature of PODS®-BDNF results in a concentration gradient over  
574     the course of Day 1–7 (Figure 5), resulting in the promotion of hESC-derived  
575     ONP differentiation towards SGN lineage and directed neurite extension.

576     It should be noted that our FEM assumes free diffusion of the rhBDNF

577 protein. In biological cell-culture conditions, BDNF released from PODS®-  
578 BDNF has tendency to adhere to walls of the culture device because BDNF  
579 is a "sticky" protein of about 27 kDa (mature BDNF dimer), and is positively  
580 charged under physiological conditions (isoelectric point, pI = 9.4) [60]. As such,  
581 the physio-chemical properties of BDNF have made the recombinant protein  
582 difficult to diffuse. This phenomenon was observable in preliminary data where  
583 the ONPs failed to survive past 1–3 days of culture (data not shown). To  
584 circumvent this issue we infused the culture media with a carrier protein (i.e.,  
585 BSA), hypothesizing that the albumin would act as a carrier for the released  
586 BDNF and allow for free diffusion throughout the microfluidic device [61]. This  
587 hypothesis is supported by our sets of biological verification data (Figures 7–11)  
588 that clearly shows that hPSC-derived ONPs responded to the modification by  
589 exhibiting the expected cell body orientation, unidirectional neurite extension,  
590 and neurite length. Note that albumin is the single protein found in highest  
591 concentrations in the perilymph [62], therefore, a carrier protein will not be  
592 needed in our future *in vivo* study.

593 *4.4. Intracellular signaling initiated by Thyrosine kinase B receptor*

594 Another issue we need to consider in interpretation of our results is the intra-  
595 cellular cell signaling mechanism elicited by rhBDNF. Human BDNF (mature  
596 dimeric form) binds with high affinity to its TrkB receptor. The binding of  
597 BDNF to a TrkB receptor has proven to have significant importance for the  
598 proneuronal effects of BDNF [20]. Upon binding BDNF, TrkB dimerizes, and  
599 activates intrinsic kinase activities and other complex set of intracellular sig-  
600 naling cascades, which is beyond the scope of this study. However, it should  
601 be noted that activation of TrkB receptor by neurotrophin binding causes the  
602 TrkB protein to be internalized in endosomes on the cellular membrane [63].  
603 Endosomes can then be transported to the soma. Therefore, the proneuronal  
604 effects of rhBDNF in our results might have highly depended on the status of  
605 TrkB receptors on the cell membrane of hPSC-derived ONPs. Our previous  
606 study has demonstrated that strong expression of a TrkB receptor on derived

607 ONPs [24], however, more detailed studies on TrkB receptors on hPSC-derived  
608 ONP and SGNs will be needed.

609 *4.5. Degradation of PODS® crystals by protease*

610 In cell culture, degradation of PODS®-rhBDNF is likely due to the activity  
611 of cell-secreted proteases. The proteases break down the peptide bonds of the  
612 encasing polyhedrin protein, creating openings in the structure to allow release  
613 of the rhBDNF. Therefore, the presence of proteases is imperative for the proper  
614 utilization of the PODS® crystals. Additionally, these proteases are responsible  
615 for the degradation of the released BDNF. Because stem cells are not present  
616 in the culture media used for the PODS® degradation kinetics experiments, we  
617 infused the media with 10% FBS, which naturally contains proteases, to promote  
618 polyhedrin degradation, BDNF release, and BDNF degradation to attain results  
619 that more accurately describe *in vitro* events. Moreover, since the cells and  
620 PODS are initially segregated into separate compartments within the culture  
621 device, cell-secreted proteases are unlikely to reach and degrade the PODS in  
622 time to support ONP survival and differentiation. Infusion of FBS was therefore  
623 required in these experiments as well. In clinical use, however, we presume  
624 that cell-secreted proteases will be readily present in the inner ear and would  
625 therefore preclude the need for artificial supplementation.

626 *4.6. A concept design: Neurotrophic strip*

627 The plateau in CI performance in treatment of sensorineural hearing loss has  
628 driven researchers to develop innovative supplementary treatment strategies to  
629 push the field past this hurdle. Our approach strives to directly address the  
630 issue at its core: the electrode-neuron gap, which can lead to serious implica-  
631 tions include low spatial frequency resolution and high power consumption. We  
632 can use our data as a launchpad for the neurotrophic strip (NS). The NS is a  
633 biointerface concept that integrates an extended-release source of growth factor  
634 to facilitate a protein gradient. Implanted in conjunction with the CI, it acts  
635 as a bridge between the extant SGNs and implanted late-ONPs grown on the

636 electrode itself. The NS would promote survival of both cell populations, dif-  
637 ferentiation of the late ONP implants, promote directional neurite growth and  
638 synaptogenesis between the two, effectively creating a neuronal network between  
639 the patient and the implanted CI. Each electrode would be able to stimulate cell  
640 bodies at exceptionally high resolution, essential for greater intonation differ-  
641 entiability (required for effective social interaction and music appreciation) and  
642 so, increased quality of life for millions. Our successful outcomes are essential  
643 to make a neurotrophic strip feasible in *in vivo* environment.

644 *4.7. The limitations of this study and future direction*

645 There are some limitations associated with this study. First, the reduction of  
646 spacial dimension to 2D for diffusion modeling certainly affected the flux vector,  
647 which determines the predicted concentration vector. Given that the thickness  
648 (i.e., Z-axis) of the microfluidic device was 100  $\mu\text{m}$ , we estimated that the effect  
649 was minimal. In the future, we plan to use PSC-derived 3D spheroids in a somal  
650 compartment so that flux vector and concentration gradient vector can more  
651 accurately model the cell behavior. In this way, we will be able to circumvent  
652 the need to reduce diffusion calculations to 2D for computation performance in  
653 the modeling.

654 Secondly, we required to generate a model in that the BDNF's biological  
655 transportation phenomenon from a PODS®-rhBDNF disc to a somal compart-  
656 ment of a Xona™ device. Note that in this model, we focused on the major  
657 dependent variable, BDNF concentration gradient to model the biological phe-  
658 nomenon. Other physical variables to promote cell migration, otic neuronal  
659 differentiation, and neurite growth were not take into consideration. These  
660 variables include electotaxis (electrical potential), durotaxis (matrix's stiffness  
661 [i.e., laminin 511 in our case]) [64], mechanotaxis (cell strain), and lastly cell  
662 migration by random walk [65]. In our future study, we will take these vari-  
663 ables into consideration to more accurately represent the migration and neurite  
664 growth of hPSC-derived ONPs.

665 Insufficient contrast between cells and background in phase contrast images

666 led to inaccuracies in cell orientation computation for some images. To address  
667 this issue, poor quality images were disregarded in the quantitative analysis.  
668 We occasionally used manual measurement for accuracy. Our future study may  
669 entail automated time-series cell analysis, which would allow more accurate  
670 measurement. Also, another way to address this issue would be with a cell  
671 membrane staining in the future.

672 While 20,000 of PODS®-rhBDNF were necessary for hPSC-derived ONPs  
673 for otic neuronal differentiation and directional neurite outgrowth, this condition  
674 may not be sufficient. For instance, it is still not known whether the effects  
675 of other neurotrophic factors such as Neurotrophin-3 and Glial cell line-derived  
676 neurotrophic factor could have a positive effect on ONP growth [20, 66, 67]. We  
677 are planning to investigate these neurotrophic factors in the future. Other fac-  
678 tors that could have an impact on directional neurite growth include endogenous  
679 factors secreted from hPSC-derived ONPs. While our previous study demon-  
680 strated that hPSC-derived ONPs only secreted negligible amount of BDNF that  
681 were detected by ELISA [9], currently we do not have any data on other neu-  
682 rotrophic factors or other molecules that could have affected directional neurite  
683 growth in the inner ear. We chose BDNF first to study because the most inten-  
684 sively studied neurotrophic factor in the field of hearing research is BDNF [20].  
685 Previous studies have indicated that neurotrophic supports of SGNs are mainly  
686 from BDNF and neurotrophin-3 (NT-3) [20, 60]. Therefore, the potential con-  
687 founding effect of the secretions of other neurotrophic factors and molecules  
688 secreted from derived SGNs are likely NT-3, for which further investigation is  
689 necessary in the future.

690 Despite the aforementioned limitations associated in this study, the present  
691 results generated BDNF concentration gradient, condition of which is necessary  
692 for hPSC-derived ONPs to differentiate into the otic lineage (i.e., SGNs) and  
693 also promoted directional neurite extension towards the POD-BDNF disc. The  
694 technique will allow us to control neurite direction of transplanted hPSC-derived  
695 ONPs in the inner ear. We will harness this method in our design of a bioactive  
696 CI.

697 **Conclusions**

698 We were able to generate BDNF concentration gradient, enabling survival,  
699 neuronal differentiation toward SGNs, and directed neurite extension of hPSC-  
700 derived ONPs. The technique will allow us to control neurite direction of trans-  
701 planted hPSC-derived ONPs in the inner ear. This proof-of-concept study pro-  
702 vides a step toward next-generation bioacitve CI technology.

703 **Acknowledgment**

704 This work was supported by the American Otological Society Clinician Sci-  
705 entist Award (AJM), the Triological Society/American College of Surgeons  
706 Clinician Scientist Award (AJM), the Department of Otolaryngology of North-  
707 western University (AJM), the NIH (NIDCD) K08 Clinician Scientist Award  
708 K08DC13829-02 (AJM), and the Office of the Assistant Secretary of Defense of  
709 Health Affairs through the Hearing Restoration Research Program (Award #:  
710 RH170013:WU81XWUH-18-0712). Imaging work was performed at the North-  
711 western University Center for Advanced Microscopy, which is generously sup-  
712 ported by NCI CCSG P30 CA060553 awarded to the Robert H. Lurie Com-  
713 prehensive Cancer Center, for which we thank Peter Dluhy, Constadina Ar-  
714 vanitis, Ph.D., David Kirchenbuechler, Ph.D., and Wensheng (Wilson) Liu,  
715 M.D. Some of microfluidic device experiments were performed in the Analytical  
716 bioNanoTechnology (ANTEC) Core Facility of the Simpson Querrey Institute  
717 at Northwestern University, which is supported by the Soft and Hybrid Nan-  
718 otechnology Experimental (SHyNE) Resource (NSFECCS-1542205). We thank  
719 Shreyas Bharadwaj (Cornell University), Kyle Coots (Midwestern University),  
720 Andrew Oleksijew (the University of Nebraska), Duncan Chadly (California In-  
721 stitute of Technology), and Shun Kobayashi (the University of Texas at Austin)  
722 for their contribution to the earlier phases of this project. We thank Sara Dun-  
723 lop (Department of Neurology, Northwestern University), and Dr. Jacqueline  
724 Bond (the University of California San Diego) for assistance in Western Blot and

725 SDS-Page gels. We also thank Dr. Georgia Minakaki (Department of Neurology,  
726 Northwestern University) on assistance in ELISA. Finally, our thanks and  
727 appreciation go to our collaborator, Dr. Christian Pernstich (Cell Guidance  
728 Systems), for continuous support and stimulating discussions on this project  
729 since 2015.

730 **References**

- 731 [1] J. G. Naples, M. J. Ruckenstein, Cochlear Implant., Otolaryngologic Clinics  
732 of North America 53 (1) (2020) 87–102. [doi:10.1016/j.otc.2019.09.004](https://doi.org/10.1016/j.otc.2019.09.004).
- 734 [2] B. S. Wilson, M. F. Dorman, Cochlear implants: A remarkable past  
735 and a brilliant future, Hearing Research 242 (1-2) (2008) 3–21. [arXiv:  
736 NIHMS150003](https://arxiv.org/abs/150003), [doi:10.1016/j.heares.2008.06.005](https://doi.org/10.1016/j.heares.2008.06.005).
- 737 [3] C. Frick, M. Müller, U. Wank, A. Tropitzsch, B. Kramer, P. Senn, H. Rask-  
738 Anderson, K. H. Wiesmüller, H. Löwenheim, Biofunctionalized peptide-  
739 based hydrogels provide permissive scaffolds to attract neurite outgrowth  
740 from spiral ganglion neurons, Colloids and Surfaces B: Biointerfaces 149  
741 (2017) 105–114. [doi:10.1016/j.colsurfb.2016.10.003](https://doi.org/10.1016/j.colsurfb.2016.10.003).
- 742 [4] S. Hahnewald, A. Tscherter, E. Marconi, J. Streit, H. R. Widmer, C. Gar-  
743 nham, H. Benav, M. Mueller, H. Löwenheim, M. Roccio, P. Senn, Response  
744 profiles of murine spiral ganglion neurons on multi-electrode arrays., Journal  
745 of neural engineering 13 (1) (2016) 16011. [doi:10.1088/1741-2560/  
746 13/1/016011](https://doi.org/10.1088/1741-2560/13/1/016011).
- 747 [5] R. K. Shepherd, S. Hatsushika, G. M. Clark, Electrical stimulation of  
748 the auditory nerve: The effect of electrode position on neural excitation,  
749 Hearing Research 66 (1) (1993) 108–120. [doi:10.1016/0378-5955\(93\)90265-3](https://doi.org/10.1016/0378-5955(93)<br/>750 90265-3).
- 751 [6] M. Tykocinski, L. T. Cohen, B. C. Pyman, T. Roland, C. Treaba, J. Palamara,  
752 M. C. Dahm, R. K. Shepherd, J. Xu, R. S. Cowan, N. L. Cohen,

- 753 G. M. Clark, Comparison of electrode position in the human cochlea using  
754 various perimodiolar electrode arrays., *The American journal of otology*  
755 21 (2) (2000) 205–211. doi:10.1016/S0196-0709(00)80010-1.
- 756 [7] A. Roemer, U. Köhl, O. Majdani, S. Klöß, C. Falk, S. Haumann, T. Lenarz,  
757 A. Kral, A. Warnecke, Biohybrid cochlear implants in human neurosensory  
758 restoration., *Stem cell research and therapy* 7 (1) (2016) 148. doi:10.  
759 1186/s13287-016-0408-y.
- 760 [8] R. A. Heuer, K. T. Nella, H. T. Chang, K. S. Coots, A. M. Oleksijew,  
761 C. B. Roque, L. H. Silva, T. L. McGuire, K. Homma, A. J. Matsuoka,  
762 Three-dimensional otic neuronal progenitor spheroids derived from human  
763 embryonic stem cells, *Tissue Engineering - Part A* 27 (3-4) (2021) 256–269.  
764 doi:10.1089/ten.tea.2020.0078.
- 765 [9] H.-T. Chang, R. A. Heuer, A. M. Oleksijew, K. S. Coots, C. B. Roque, K. T.  
766 Nella, T. L. McGuire, A. J. Matsuoka, An Engineered Three-Dimensional  
767 Stem Cell Niche in the Inner Ear by Applying a Nanofibrillar Cellulose  
768 Hydrogel with a Sustained-Release Neurotrophic Factor Delivery System,  
769 *Acta Biomaterialia* 108 (2020) 111–127. doi:<https://doi.org/10.1016/j.actbio.2020.03.007>.
- 771 [10] L. Taylor, L. Jones, M. H. Tuszyński, A. Blesch, Neurotrophin-3 gradients  
772 established by lentiviral gene delivery promote short-distance axonal bridg-  
773 ing beyond cellular grafts in the injured spinal cord, *Journal of Neuroscience*  
774 26 (38) (2006) 9713–9721. doi:10.1523/JNEUROSCI.0734-06.2006.
- 775 [11] P. Senn, M. Roccio, S. Hahnewald, C. Frick, M. Kwiatkowska, M. Ishikawa,  
776 P. Bako, H. Li, F. Edin, W. Liu, H. Rask-Andersen, I. Pyykkö, J. Zou,  
777 M. Mannerström, H. Keppner, A. Homsy, E. Laux, M. Llera, J. P. Lel-  
778 louche, S. Ostrovsky, E. Banin, A. Gedanken, N. Perkas, U. Wank, K. H.  
779 Wiesmüller, P. Mistrík, H. Benav, C. Garnham, C. Jolly, F. Gander, P. Ul-  
780 rich, M. Müller, H. Löwenheim, NANOCI-Nanotechnology Based Cochlear

- 781      Implant with Gapless Interface to Auditory Neurons, *Otology and Neuro-*  
782      *tology* 38 (8) (2017) e224—e231. doi:10.1097/MAO.0000000000001439.
- 783      [12] G. J. Goodhill, H. Baier, Axon Guidance: Stretching Gradients to  
784      the Limit, *Neural Computation* 10 (3) (1998) 521–527. doi:10.1162/  
785      089976698300017638.
- 786      [13] L. N. Gillespie, G. M. Clark, P. F. Bartlett, P. L. Marzella, BDNF-induced  
787      survival of auditory neurons *in vivo*: Cessation of treatment leads to ac-  
788      celerated loss of survival effects, *Journal of Neuroscience Research* 71 (6)  
789      (2003) 785–790. doi:10.1002/jnr.10542.
- 790      [14] L. N. Pettingill, R. L. Minter, R. K. Shepherd, Schwann cells geneti-  
791      cally modified to express neurotrophins promote spiral ganglion neuron  
792      survival *in vitro*, *Neuroscience* 152 (3) (2008) 821–828. doi:10.1016/j.  
793      neuroscience.2007.11.057.Schwann.
- 794      [15] R. K. Shepherd, A. Coco, S. B. Epp, Neurotrophins and electrical stim-  
795      ulation for protection and repair of spiral ganglion neurons following  
796      sensorineural hearing loss, *Hearing Research* 242 (2009) 100–109. doi:  
797      10.1016/j.heares.2007.12.005.Neurotrophins.
- 798      [16] B. Baseri, J. J. Choi, T. Deffieux, G. Samiotaki, Y. S. Tung, O. Olu-  
799      molade, S. A. Small, B. Morrison, E. E. Konofagou, Activation of sig-  
800      naling pathways following localized delivery of systemically administered  
801      neurotrophic factors across the bloodbrain barrier using focused ultra-  
802      sound and microbubbles, *Physics in Medicine and Biology* 57 (7). doi:  
803      10.1088/0031-9155/57/7/N65.
- 804      [17] K. Ikeda, S. Nagaoka, S. Winkler, K. Kotani, H. Yagi, K. Nakanishi,  
805      S. Miyajima, J. Kobayashi, H. Mori, Molecular Characterization of Bom-  
806      byx mori Cytoplasmic Polyhedrosis Virus Genome Segment 4, *Journal of*  
807      *Virology* 75 (2) (2001) 988–995. doi:10.1128/jvi.75.2.988–995.2001.

- 808 [18] T. Suzuki, T. Kanaya, H. Okazaki, K. Ogawa, A. Usami, H. Watanabe,  
809 K. Kadono-Okuda, M. Yamakawa, H. Sato, H. Mori, S. Takahashi, K. Oda,  
810 Efficient protein production using a Bombyx mori nuclear polyhedrosis  
811 virus lacking the cysteine proteinase gene, *Journal of General Virology*  
812 78 (12) (1997) 3073–3080. doi:10.1099/0022-1317-78-12-3073.
- 813 [19] H. Mori, R. Ito, H. Nakazawa, M. Sumida, F. Matsubara, Y. Minobe,  
814 Expression of Bombyx mori cytoplasmic polyhedrosis virus polyhedrin in  
815 insect cells by using a baculovirus expression vector, and its assembly into  
816 polyhedra, *Journal of General Virology* 74 (1) (1993) 99–102. doi:10.  
817 1099/0022-1317-74-1-99.
- 818 [20] S. H. Green, E. Bailey, Q. Wang, R. L. Davis, The Trk A, B, C's of  
819 Neurotrophins in the Cochlea., *Anatomical record* (Hoboken, N.J. : 2007)  
820 295 (11) (2012) 1877–1895. doi:10.1002/ar.22587.
- 821 [21] I. Meyvantsson, D. J. Beebe, Cell culture models in microfluidic systems,  
822 *Annual Review of Analytical Chemistry* 1 (1) (2008) 423–449. doi:10.  
823 1146/annurev.anchem.1.031207.113042.
- 824 [22] Z.-J. Guo, M.-H. Yu, X.-Y. Dong, W.-L. Wang, T. Tian, X.-Y. Yu, X.-D.  
825 Tang, Protein composition analysis of polyhedra matrix of Bombyx mori  
826 nucleopolyhedrovirus (BmNPV) showed powerful capacity of polyhedra to  
827 encapsulate foreign proteins., *Scientific reports* 7 (1) (2017) 8768. doi:  
828 10.1038/s41598-017-08987-8.
- 829 [23] A. J. Matsuoka, Z. A. Sayed, N. Stephanopoulos, E. J. Berns, A. R. Wad-  
830 hwani, Z. D. Morrissey, D. M. Chedly, S. Kobayashi, A. N. Edelbrock,  
831 T. Mashimo, C. A. Miller, T. L. McGuire, S. I. Stupp, J. A. Kessler,  
832 Creating a stem cell niche in the inner ear using self-assembling peptide  
833 amphiphiles., *Plos One* 12 (12) (2017) e0190150. doi:10.1371/journal.  
834 pone.0190150.
- 835 [24] A. J. Matsuoka, Z. D. Morrissey, C. Zhang, K. Homma, A. Belmadani,

- 836 C. A. Miller, D. M. Chadly, S. Kobayashi, A. N. Edelbrock, M. Tanaka-  
837 Matakatsu, D. S. Whitlon, L. Lyass, T. L. McGruire, S. I. Stupp, J. A.  
838 Kessler, Directed Differentiation of Human Embryonic Stem Cells Toward  
839 Placode-Derived Spiral Ganglion-Like Sensory Neurons, *Stem Cells Trans-  
840 lational Medicine* 6 (2017) 923–936. doi:10.1002/sctm.16-0032.
- 841 [25] H. Al-Ali, S. R. Beckerman, J. L. Bixby, V. P. Lemmon, In vitro models  
842 of axon regeneration, *Experimental Neurology* 287 (Pt 3) (2017) 423–434.  
843 doi:10.1016/j.expneurol.2016.01.020.
- 844 [26] U. K. Laemmli, Cleavage of structural proteins during the assembly of  
845 the head of bacteriophage T4., *Nature* 227 (5259) (1970) 680–685. doi:  
846 10.1038/227680a0.
- 847 [27] A. L. Mandel, H. Ozdener, V. Utermohlen, Identification of pro- and mature  
848 brain-derived neurotrophic factor in human saliva., *Archives of oral biology*  
849 54 (7) (2009) 689–695. doi:10.1016/j.archoralbio.2009.04.005.
- 850 [28] C. A. Schneider, W. S. Rasband, K. W. Eliceiri, NIH Image to ImageJ:  
851 25 years of image analysis, *Nature Methods* 9 (7) (2012) 671–675. arXiv:  
852 arXiv:1011.1669v3, doi:10.1038/nmeth.2089.
- 853 [29] R. W. Burry, Controls for immunocytochemistry: an update., *The journal*  
854 *of histochemistry and cytochemistry : official journal of the Histochemistry*  
855 *Society* 59 (1) (2011) 6–12. doi:10.1369/jhc.2010.956920.
- 856 [30] M. B. Mazalan, M. A. B. Ramlan, J. H. Shin, T. Ohashi, Effect of geomet-  
857 ric curvature on collective cell migration in tortuous microchannel devices,  
858 *Micromachines* 11 (7) (2020) 1–17. doi:10.3390/MI11070659.
- 859 [31] F. Xu, T. Beyazoglu, E. Hefner, U. A. Gurkan, U. Demirci, Automated  
860 and adaptable quantification of cellular alignment from microscopic images  
861 for tissue engineering applications, *Tissue Engineering - Part C: Methods*  
862 17 (6) (2011) 641–649. doi:10.1089/ten.tec.2011.0038.

- 863 [32] E. Batschelet, Circular Statistics in Biology (Mathematics in Biology Series),  
864 1st Edition, Academic Press, New York, NY, 1981.
- 865 [33] P. Berens, M. J. Velasco, CircStat for Matlab: Toolbox for circular statistics  
866 with Matlab, Max–Planck–Institut f ur biologische Kybernetik, Technical  
867 Report No. 184 31 (10) (2009) 1–21. doi:[doi:10.18637/jss.v031.i10](https://doi.org/10.18637/jss.v031.i10).
- 868 [34] M. Pool, J. Thiemann, A. Bar-Or, A. E. Fournier, NeuriteTracer: A novel  
869 ImageJ plugin for automated quantification of neurite outgrowth, Journal  
870 of Neuroscience Methods 168 (1) (2008) 134–139. doi:[10.1016/j.jneumeth.2007.08.029](https://doi.org/10.1016/j.jneumeth.2007.08.029).
- 872 [35] E. Meijering, M. Jacob, J.-C. F. Sarria, P. Steiner, H. Hirling, M. Unser,  
873 Design and validation of a tool for neurite tracing and analysis in fluo-  
874 rescence microscopy images., Cytometry. Part A : the journal of the In-  
875 ternational Society for Analytical Cytology 58 (2) (2004) 167–176. doi:  
876 [10.1002/cyto.a.20022](https://doi.org/10.1002/cyto.a.20022).
- 877 [36] M. Anniko, W. Arnold, T. Stigbrand, A. Strom, The Human Spiral Gan-  
878 glion, ORL 57 (1995) 68–77.
- 879 [37] S. van der Walt, S. C. Colbert, G. Varoquaux, The NumPy Array: A  
880 Structure for Efficient Numerical Computation, Computing in Science En-  
881 gineering 13 (2) (2011) 22–30. doi:[10.1109/MCSE.2011.37](https://doi.org/10.1109/MCSE.2011.37).
- 882 [38] J. D. Hunter, Matplotlib: A 2D Graphics Environment, Computing in  
883 Science Engineering 9 (3) (2007) 90–95. doi:[10.1109/MCSE.2007.55](https://doi.org/10.1109/MCSE.2007.55).
- 884 [39] P. Virtanen, R. Gommers, T. E. Oliphant, M. Haberland, T. Reddy,  
885 D. Cournapeau, E. Burovski, P. Peterson, W. Weckesser, J. Bright, S. J.  
886 van der Walt, M. Brett, J. Wilson, K. J. Millman, N. Mayorov, A. R. J.  
887 Nelson, E. Jones, R. Kern, E. Larson, C. J. Carey, I. Polat, Y. Feng,  
888 E. W. Moore, J. VanderPlas, D. Laxalde, J. Perktold, R. Cimrman, I. Hen-  
889 riksen, E. A. Quintero, C. R. Harris, A. M. Archibald, A. H. Ribeiro,  
890 F. Pedregosa, P. van Mulbregt, SciPy 1.0: fundamental algorithms for

- 891 scientific computing in Python., *Nature methods* 17 (3) (2020) 261–272.  
892 doi:10.1038/s41592-019-0686-2.
- 893 [40] P. Berens, CircStat : A MATLAB Toolbox for Circular Statistics , *Journal*  
894 of Statistical Software
- 895 [41] M. Tuncel, H. S. Sürütü, K. M. Erbil, A. Konan, Formation of the cochlear  
896 nerve in the modiolus of the guinea pig and human cochleae., *Archives of*  
897 *medical research* 36 (5) (2005) 436–40. doi:10.1016/j.arcmed.2005.02.  
898 003.
- 899 [42] B. Küçük, K. Abe, T. Ushiki, Y. Inuyama, S. Fukuda, Kazuo Ishikawa,  
900 Microstructures of the Bony Modiolus in the Human Cochlea : A Scanning  
901 Electron Microscopic Study, *Journal of Electron Microsc* 40 (40) (1991)  
902 193–197.
- 903 [43] O. Levenspiel, *Chemical Reaction Engineering*, 3rd Edition, John Wiley  
904 and Sons, Inc., New York, NY, 1999.
- 905 [44] M. Stroh, W. R. Zipfel, R. M. Williams, S. C. Ma, W. W. Webb, W. M.  
906 Saltzman, Multiphoton microscopy guides neurotrophin modification with  
907 poly(ethylene glycol) to enhance interstitial diffusion, *Nature Materials*  
908 3 (7) (2004) 489–494. doi:10.1038/nmat1159.
- 909 [45] S. Axler, *Linear Algebra Done Right*, 3rd Edition, Springer Publishing,  
910 New York, NY, 2015.
- 911 [46] J. Crank, *The mathematics of Diffusion*, 2nd Edition, Oxford University  
912 Press, London, UK, 1979.
- 913 [47] K. M. Keefe, I. S. Sheikh, G. M. Smith, Targeting Neurotrophins to Specific  
914 Populations of Neurons: NGF, BDNF, and NT-3 and Their Relevance  
915 for Treatment of Spinal Cord Injury., *International journal of molecular*  
916 *sciences* 18 (3). doi:10.3390/ijms18030548.

- 917 [48] B. I. Awad, M. A. Carmody, M. P. Steinmetz, Potential role of growth  
918 factors in the management of spinal cord injury., *World Neurosurgery* 83 (1)  
919 (2015) 120–131. doi:[10.1016/j.wneu.2013.01.042](https://doi.org/10.1016/j.wneu.2013.01.042).
- 920 [49] E. R. n. Hollis, M. H. Tuszyński, Neurotrophins: potential therapeutic tools  
921 for the treatment of spinal cord injury., *Neurotherapeutics : the journal of*  
922 *the American Society for Experimental NeuroTherapeutics* 8 (4) (2011)  
923 694–703. doi:[10.1007/s13311-011-0074-9](https://doi.org/10.1007/s13311-011-0074-9).
- 924 [50] A. H. Nagahara, B. R. Wilson, I. Ivasyk, I. Kovacs, S. Rawalji, J. R.  
925 Bringas, P. J. Piviroto, W. S. Sebastian, L. Samaranch, K. S. Bankiewicz,  
926 M. H. Tuszyński, MR-guided delivery of AAV2-BDNF into the entorhi-  
927 nal cortex of non-human primates., *Gene therapy* 25 (2) (2018) 104–114.  
928 doi:[10.1038/s41434-018-0010-2](https://doi.org/10.1038/s41434-018-0010-2).
- 929 [51] S. D. Croll, C. Suri, D. L. Compton, M. V. Simmons, G. D. Yan-  
930 copoulos, R. M. Lindsay, S. J. Wiegand, J. S. Rudge, H. E. Scharfman,  
931 Brain-derived neurotrophic factor transgenic mice exhibit passive avoid-  
932 ance deficits, increased seizure severity and in vitro hyperexcitability in  
933 the hippocampus and entorhinal cortex., *Neuroscience* 93 (4) (1999) 1491–  
934 1506. doi:[10.1016/s0306-4522\(99\)00296-1](https://doi.org/10.1016/s0306-4522(99)00296-1).
- 935 [52] A. Dravid, S. Parittotokkaporn, Z. Aqrawe, S. J. O’Carroll, D. Svirskis,  
936 Determining Neurotrophin Gradients in Vitro to Direct Axonal Outgrowth  
937 following Spinal Cord Injury, *ACS Chemical Neuroscience* 11 (2) (2020)  
938 121–132. doi:[10.1021/acschemneuro.9b00565](https://doi.org/10.1021/acschemneuro.9b00565).
- 939 [53] T. Yamagata, J. M. Miller, M. Ulfendahl, N. P. Olivius, R. A. Altschuler,  
940 I. Pyykkö, G. Bredberg, Delayed neurotrophic treatment preserves nerve  
941 survival and electrophysiological responsiveness in neomycin-deafened  
942 guinea pigs., *Journal of neuroscience research* 78 (1) (2004) 75–86. doi:  
943 doi:[10.1002/jnr.20239](https://doi.org/10.1002/jnr.20239).
- 944 [54] M. P. Zanin, M. Hellstr??m, R. K. Shepherd, A. R. Harvey, L. N. Gillespie,

- 945 Development of a cell-based treatment for long-term neurotrophin expres-  
946 sion and spiral ganglion neuron survival, *Neuroscience* 277 (2014) 690–699.  
947 doi:10.1016/j.neuroscience.2014.07.044.
- 948 [55] M. Seyyedi, L. Viana, J. J. Nadol, Within-subject comparison of word  
949 recognition and spiral ganglion cell count in bilateral cochlear implant  
950 recipients, *Otol Neurotol* 35 (8) (2014) 1446–1450. doi:10.1097/MAO.  
951 000000000000443.Within-Subject.
- 952 [56] A. Henriques, C. Pitzer, A. Schneider, Neurotrophic growth factors for the  
953 treatment of amyotrophic lateral sclerosis: where do we stand?, *Frontiers*  
954 in neuroscience
- 4 (2010) 32. doi:10.3389/fnins.2010.00032.
- 955 [57] J. F. Poduslo, G. L. Curran, Permeability at the blood-brain and  
956 blood-nerve barriers of the neurotrophic factors: NGF, CNTF, NT-3,  
957 BDNF, *Molecular Brain Research* 36 (2) (1996) 280–286. doi:10.1016/  
958 0169-328X(95)00250-V.
- 959 [58] T. Sakane, W. M. Pardridge, Carboxyl-directed pegylation of brain-derived  
960 neurotrophic factor markedly reduces systemic clearance with minimal loss  
961 of biologic activity (1997). doi:10.1023/A:1012117815460.
- 962 [59] R. G. Soderquist, E. D. Milligan, E. M. Sloane, J. A. Harrison, K. K.  
963 Douvas, J. M. Potter, T. S. Hughes, R. A. Chavez, K. Johnson, L. R.  
964 Watkins, M. J. Mahoney, PEGylation of brain-derived neurotrophic factor  
965 for preserved biological activity and enhanced spinal cord distribution.,  
966 *Journal of biomedical materials research. Part A* 91 (3) (2009) 719–729.  
967 doi:10.1002/jbm.a.32254.
- 968 [60] M. Sasi, B. Vignoli, M. Canossa, R. Blum, Neurobiology of local and inter-  
969 cellular BDNF signaling, *Pflugers Archiv : European journal of physiology*  
970 469 (5-6) (2017) 593–610. doi:10.1007/s00424-017-1964-4.
- 971 [61] X. Li, Y. Su, S. Liu, L. Tan, X. Mo, S. Ramakrishna, Encapsulation  
972 of proteins in poly(l-lactide-co-caprolactone) fibers by emulsion electro-

- 973 spinning, *Colloids and Surfaces B: Biointerfaces* 75 (2) (2010) 418–424.  
974 [doi:10.1016/j.colsurfb.2009.09.014](https://doi.org/10.1016/j.colsurfb.2009.09.014).
- 975 [62] E. E. L. Swan, M. Peppi, Z. Chen, K. M. Green, J. E. Evans, M. J.  
976 McKenna, M. J. Mescher, S. G. Kujawa, W. F. Sewell, Proteomics analysis  
977 of perilymph and cerebrospinal fluid in mouse., *The Laryngoscope* 119 (5)  
978 (2009) 953–958. [doi:10.1002/lary.20209](https://doi.org/10.1002/lary.20209).
- 979 [63] T. Numakawa, S. Suzuki, E. Kumamaru, N. Adachi, M. Richards,  
980 H. Kunugi, BDNF function and intracellular signaling in neurons, *Histology  
981 and Histopathology* 25 (2) (2010) 237–258. [doi:10.14670/HH-25.237](https://doi.org/10.14670/HH-25.237).
- 982 [64] C. Gentile, Engineering of Spheroids for Stem Cell Technology, *Current  
983 Stem Cell Research & Therapy* 11 (2016) 652–665. [doi:10.2174/1574888x10666151001114848](https://doi.org/10.2174/1574888x10666151001114848).
- 985 [65] H. Berg, *Random Walks in Biology*, Princeton Universtiy Press, Prinston,  
986 NJ, 1983.
- 987 [66] H. Li, F. Edin, H. Hayashi, O. Gudjonsson, N. Danckwardt-Lillies, H. En-  
988 gqvist, H. Rask-Andersen, W. Xia, Guided growth of auditory neurons:  
989 Bioactive particles towards gapless neural electrode interface, *Biomaterials*  
990 122 (2017) 1–9. [doi:10.1016/j.biomaterials.2016.12.020](https://doi.org/10.1016/j.biomaterials.2016.12.020).
- 991 [67] J. Schulze, H. Staeker, D. Wedekind, T. Lenarz, A. Warnecke, Expression  
992 pattern of brain-derived neurotrophic factor and its associated receptors:  
993 Implications for exogenous neurotrophin application., *Hearing Research* 413  
994 (2020) 108098. [doi:10.1016/j.heares.2020.108098](https://doi.org/10.1016/j.heares.2020.108098).